A changing wave climate in the Mediterranean Sea during 58-years using UERRA-MESCAN-SURFEX high-resolution wind fields

Elshinnawy, Ahmed I.; Antolínez, Jose A.Á.

DOI
10.1016/j.oceaneng.2023.113689

Publication date
2023

Document Version
Final published version

Published in
Ocean Engineering

Citation (APA)
Elshinnawy, A. I., & Antolínez, J. A. Á. (2023). A changing wave climate in the Mediterranean Sea during 58-years using UERRA-MESCAN-SURFEX high-resolution wind fields. *Ocean Engineering*, *271*, Article 113689. https://doi.org/10.1016/j.oceaneng.2023.113689

Ocean Engineering 271 (2023) 113689

Contents lists available at ScienceDirect

Ocean Engineering

journal homepage: www.elsevier.com/locate/oceaneng

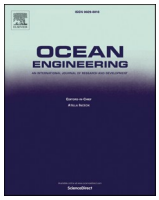

A changing wave climate in the Mediterranean Sea during 58-years using UERRA-MESCAN-SURFEX high-resolution wind fields

Ahmed I. Elshinnawy [a,c,*], Jose A.Á. Antolínez [b]

[a] Irrigation and Hydraulics Engineering Department, Faculty of Engineering, Tanta University, 31733, Tanta, Egypt
[b] Department of Hydraulic Engineering, Faculty of Civil Engineering and Geosciences, Delft University of Technology, Delft, Netherlands
[c] IHCantabria - Instituto de Hidráulica Ambiental de la Universidad de Cantabria, Avda. Isabel Torres, 15, 39011, Santander, Spain

ARTICLE INFO

Handling Editor: Prof. A.I. Incecik

Keywords:
Mediterranean Sea
Wind-waves
Climate variability
Wind-sea
Storminess
Long-term trends

ABSTRACT

This study unravels 58-years (1961–2018) of wind-waves in the Mediterranean Sea (MS). A wave dataset was developed using the wave model WAVEWATCH III forced with the high-resolution (5.5 km) UERRA-MESCAN-SURFEX downscaled wind fields which better contain the imprint of the local geomorphology compared to other, coarser wind datasets used in previous studies. Thus, improving the reliability and characterization of the wind-wave climate in the basin. Validation results revealed a higher performance than previous datasets, particularly on the wave direction (θ_m), with a bias$<1^\circ$. Climate variability at seasonal and interannual scales, wind-seas and swells distribution, and long-term trends in storminess and in the mean and extreme regimes were analysed. Results show a slight swell influence over the wind-sea in the hourly spectra at a large portion of the basin, excluding the wave generation areas. We detected that the western MS is the most storminess region with an average of three storms/year. Moreover, the anomalies of the seasonal mean wave direction relative to θ_m are large ($\sim 60^\circ$), with opposing behaviours between the winter and summer. Finally, the long-term trends in the mean and extreme conditions and in storminess are mild with values reaching 6 cm/decade and less than 2% in the absolute value, respectively.

1. Introduction

The assessment and characterization of the spatial and temporal variabilities in wind-wave climate conditions are of vital importance for all offshore, maritime, ocean, and coastal engineering applications. Examples of such applications include the design of coastal, maritime, and offshore infrastructures, such as shore-protection works, wind farms, offshore platforms, and ship routing for navigation purposes. Wave climate characterization is also important for understanding the underlying processes driving large coastal systems, such as long-term beach morphological changes (Antolínez et al., 2018; Elshinnawy et al., 2018, 2022a,b; de Schipper et al., 2021; Wiegel et al., 2021; Caloiero et al., 2022; Lira-Loarca et al., 2022). Additionally, waves contribute significantly to the overall water levels, especially during extreme events, leading to coastal erosion and flooding hazards (Melet et al., 2018; Scott et al., 2020; Toomey et al., 2022). Over the last six decades (1960–2020), annual fossil fuel carbon emissions have more than tripled, increasing from 2580 million metric tons per year in 1961 to 9885 million metric tons per year in 2014 (Boden et al., 2017). This carbon-emission increase is similar to those established in some CMIP6 experiments (Meehl et al., 2020), which are often used to investigate future wind-wave changes (Badriana and Lee, 2021; Erikson et al., 2022) that could impact human activities and coastal communities at both global and local scales (Shimura and Mori, 2019). Consequently, accurately representing and understanding both the past and present wave climate are essential and important for creating a solid reference for studying future wave climatology (Albuquerque et al., 2021; Barbariol et al., 2021; De Leo et al., 2021).

The Mediterranean Sea (MS, hereinafter) is a semi-enclosed basin between Europe and Africa (see Fig. 1). The MS represents one of the most important routes of maritime transportation in the world (Morales-Márquez et al., 2020), linking seaborne trade routes between the Atlantic Ocean and the Indian Ocean, together with the Suez Canal and the Red Sea. The MS is the most densely populated enclosed basin in the world (Lira-Loarca et al., 2022) and is characterized by complex morphological features and orography along its coastlines. In other

* Corresponding author. Irrigation and Hydraulics Engineering Department, Faculty of Engineering, Tanta University, 31733, Tanta, Egypt.
E-mail addresses: elshinnawy_im@yahoo.com, elshinnawy_im@f-eng.tanta.edu.eg, ahmed.elshinnawy@unican.es (A.I. Elshinnawy), j.a.a.antolinez@tudelft.nl (J.A.Á. Antolínez).

https://doi.org/10.1016/j.oceaneng.2023.113689
Received 31 October 2022; Received in revised form 23 December 2022; Accepted 10 January 2023
Available online 31 January 2023

words, the basin represents a regime under which sea–land boundaries and orographic features affect the flow patterns of the meteorological conditions, i.e., the overall wind fields in the area (Mentaschi et al., 2015; Cavaleri et al., 2018).

Throughout the literature, studies have often characterized the wave climate in the MS basin using wave datasets produced with third-generation spectral wave models (e.g., WAVEWATCH III, WW3DG, 2019; WAM, WAMDI Group, 1988; Bidlot et al., 2007; MIKE21-SW, Sorensen et al., 2004; or SWAN, Booij et al., 1999) forced with winds from global atmospheric reanalysis products (e.g., Barbariol et al., 2021; Elkut et al., 2021) at resolutions between 25 and 80 km and, less frequently, using downscaled regional wind fields with spatial resolutions of approximately 10 km (e.g., Mentaschi et al., 2015; Donatini et al., 2015; Lira-Loarca et al., 2022). In addition, some previous studies focused on regional analyses of the eastern MS basin (EMS) wave climate (e.g., Musić and Nicković, 2008; Ayat, 2013), while others analysed the climate variability of the western MS basin (WMS) (e.g., Ponce de León and Guedes Soares, 2008; Martínez-Asensio et al., 2013; Gonçalves et al., 2018; Vannucchi et al., 2021; Amarouche et al., 2019, 2020, 2021, 2022a, b).

Global atmospheric reanalyses, such as the Climate Forecast System Reanalysis (CFSR) (Saha et al., 2010, 2014) provided by the National Center for Environmental Prediction (NCEP) and the ERA-Interim (Dee et al., 2011) and the ERA5 (Hersbach et al., 2020) reanalyses produced by the European Center for Medium-Range Weather Forecast (ECMWF), are very useful and adequate for developing global wave hindcasts, providing reliable results at the global scale (e.g., Reguero et al., 2012; Chawla et al., 2013; Rascle and Ardhuin, 2013; Perez et al., 2017; Alday et al., 2021). However, in semi-enclosed basins such as the MS, wind fields from global reanalyses are often associated with low resolutions and are thus inaccurate in reproducing local atmospheric processes, especially those derived at meteorological timescales spanning minutes to weeks. This inadequacy is due to various factors such as the presence of complex topographic and orographic landforms, as low-resolution atmospheric reanalyses are often associated with the smoothing of sharp physical-pattern gradients; consequently, such reanalyses might be incapable of accurately representing mesoscale dynamics (Vousdoukas et al., 2017). The consequences of inputting inaccurate wind data in wave modelling include, among others, misrepresentations of the wave directionality; an incapability to mimic local waves driven by coastal breezes; underestimations of wave extremes due to wind tunnelling or convective wind effects not being accounted for; or overestimations of wind-wave energy due to a certain mountain range that might block, tunnel, or dissipate winds not being effectively captured in the numerical discretization.

These wave-modelling limitations can be addressed by using high-resolution wind fields downscaled from global or regional reanalyses. Mentaschi et al. (2015) evaluated the performance of the WAVEWATCH III (abbreviated hereinafter as WW3) wave model in the MS by forcing the model with 10-km wind fields downscaled from the CFSR reanalysis and produced a wave hindcast from 1979 to 2010. Similarly, Donatini et al. (2015) employed 10.53-km downscaled wind fields from CFSR to force the MIKE21-SW spectral model, producing a wave dataset for the 1981–2013 period. Recently, Lira-Loarca et al. (2022) followed the same approach, employing 10-km wind fields dynamically downscaled from CFSR to develop both a hindcast and a forecast for wave hazard applications in the MS.

In most of the previously mentioned studies, researchers calibrated the utilized wave datasets using short-period (days-months) measurement series collected at specific locations. Moreover, they validated the data only against buoys (e.g., Mentaschi et al., 2015; Elkut et al., 2021) or employed a small amount of altimeter data from a limited number of satellite missions (e.g., Donatini et al., 2015; Lira-Loarca et al., 2022). Furthermore, previous data validations focused on the significant wave height (H_s) and wave period but rarely on the wave directionality. For instance, in addition to using low-resolution wind fields (0.75°) from ERA-Interim, Elkut et al. (2021) calibrated and validated their wave hindcast obtained in the MS against data recorded by four buoys using one year of data corresponding to each buoy. Barbariol et al. (2021) employed surface winds from the ERA5 global reanalysis with a resolution of 0.25° to generate a hindcast in the MS without calibrating the WW3 model and validated their dataset only against satellite data. Thus,

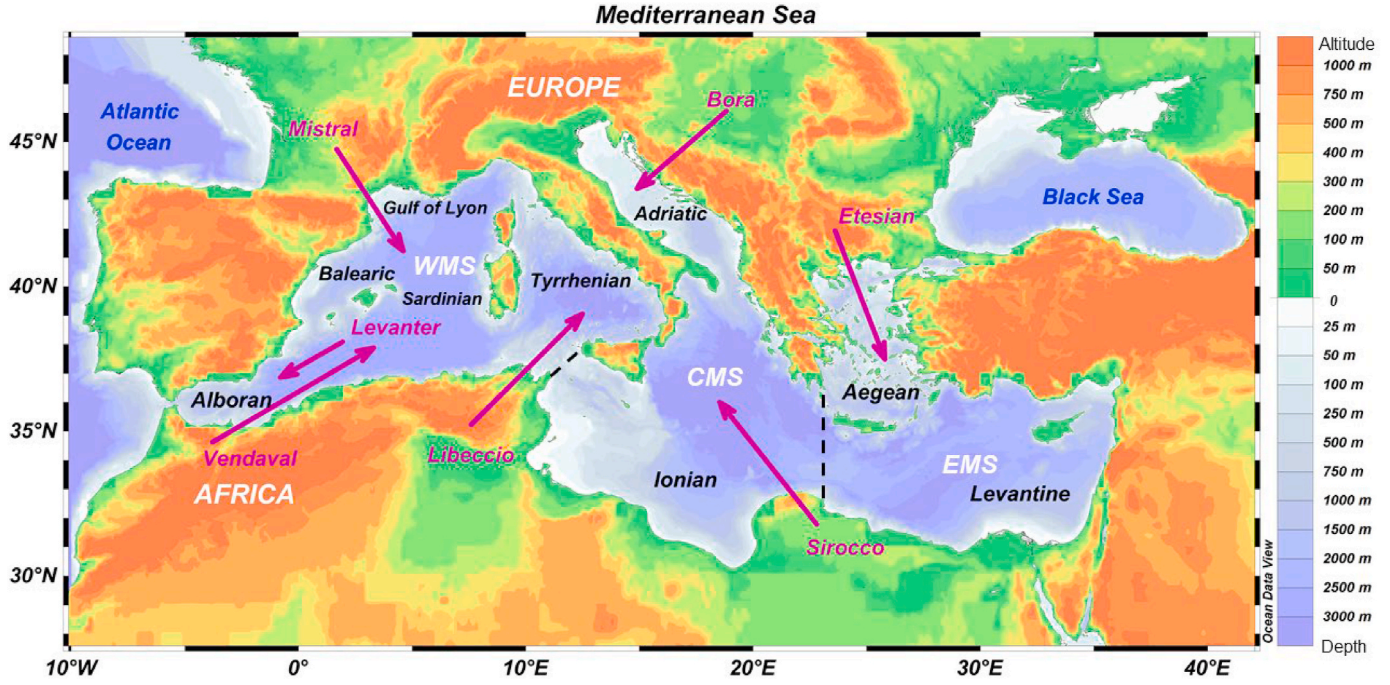

Fig. 1. The Mediterranean Sea (MS) basin and sub-basins (Levantine, Aegean, Ionian, Adriatic, Tyrrhenian, Sardinian, Balearic, and Alboran Seas). The purple arrows indicate the directions of the main wind regimes dominating the area. The dashed black lines separate the MS basin into the sub-regions (EMS: Eastern MS, CMS: Central MS, and WMS: Western MS) for the climate analysis of this study. Based on Lionello and Sanna (2005) and Barbariol et al. (2021).

the modelled H_s was underestimated overall due to the non-calibration of the wave model. Mentaschi et al. (2015) and Lira-Loarca et al. (2022) calibrated WW3 using a series of storm events, i.e., short-term wave measurements recorded during specific months. The usage of wave data corresponding to a particular month or season might lead to overfitting when calibrating wave models due to seasonality effects (Chawla et al., 2013; Stopa, 2018). Donatini et al. (2015) and Lira-loarca et al. (2022) validated their datasets in the MS using seven and eight missions, respectively, recorded in the historical GlobWave altimeter database (GlobWave, 2020). It is worth noting that newly updated and better-quality-controlled satellite datasets have been released recently with larger amounts of altimeter observations, including data from new missions (e.g., Ribal and Young, 2019; Dodet et al., 2020).

Stopa (2018) stated that atmospheric reanalysis products continually improve, and there is a need to assess their ability to reproduce wave fields. According to Li et al. (2016) and Alday et al. (2021), the quality of the numerical wave model outputs is significantly dependent on the accuracy and resolution of the forcing fields. Hence, any improvement in the quality of the wind forcing data should provide improved wave model results. Thus, employing high-resolution downscaled wind fields with spatial resolutions finer than 10 km is expected to improve the resulting wave data reliability in semi-enclosed basins such as the MS, especially regarding the wave direction results (Vannucchi et al., 2021) and extremes (Van Vledder and Akpinar, 2015; Vousdoukas et al., 2017).

Accordingly, following the evolution of and improvement in atmospheric reanalysis products, the main purpose of this study is to characterize the MS wave climate over a period spanning six decades (1961–2018) using the recently released high-resolution (5.5-km) wind fields of the UERRA-MESCAN-SURFEX regional reanalysis product constructed for Europe (Bazile et al., 2017; Ridal et al., 2017). Thus, in the current study, we investigate the intra-annual and interannual variabilities and long-term trends in the MS, thus rectifying the limitations on wave modelling referred to above. In addition to the input of high-quality wind data, the wave model is calibrated for wind-wave growth by using satellite altimeter data collected over a one-year period and employing an objective function that accounts for several percentiles defining the probability density function of H_s. Moreover, we utilize the most updated satellite altimeter observations from ten missions (Dodet et al., 2020) and all available buoy data to validate the wave dataset over a 27-year (1991–2018) period. Accordingly, this MS wave climate study relies on a long-term and high-resolution wave hindcast developed with a wave model that is fully calibrated and validated in the MS and forced by very-high-resolution wind fields.

This paper is organized into six sections. Following the introduction, in Section 2, descriptions of the study area and the different available wind fields, bathymetry and observation datasets are given. In Section 3, the model setup and calibration procedure are delineated. In Section 4, the wave dataset results are validated against buoy measurements and altimeter data. In Section 5, the characterization and analysis of the MS wave climate and its variability are presented. Finally, the main conclusions are provided in Section 6.

2. Study area and datasets

Brief descriptions of the MS basin and the available wind field, bathymetry and observation datasets in the study area are given in the following subsections.

2.1. Study area

The MS is a semi-enclosed basin located between Africa and Europe. It has a total surface area of approximately 2.5 million km^2 (Criado-Aldeanueva and Soto-Navarro, 2020) and is connected to the Black Sea to the east by the Dardanelles and Bosporus straits and to the Atlantic Ocean to the west by the Strait of Gibraltar. Its average depth is approximately 1500 m, and the sea has more than 40000 km of very highly populated coastline. The MS basin is characterized by many peninsulas and islands that divide it into eight sub-basins, i.e., the Levantine Sea, Aegean Sea, Ionian Sea, Adriatic Sea, Tyrrhenian Sea, Sardinian Sea, Balearic Sea, and Alboran Sea (see Fig. 1). Additionally, as shown in Fig. 1, several mountain ranges are located close to the MS coastline, and these mountains affect and channel the wind fields in the area, thus producing distinct local meteorological patterns. Meteorologically, the MS basin is characterized by the presence of various wind regimes that vary seasonally and among the sub-basins (Lionello and Sanna, 2005; Cavaleri et al., 2018) (see Fig. 1).

In the eastern MS (EMS) region, which includes the areas of the Aegean Sea and the Levantine Sea, northerly to north-westerly Etesian winds blow and dominate the area, with relatively strong summertime winds.

In the central MS (CMS), three wind systems dominate the area. First, the Bora winds, which consist of north-easterly dry and cold wind jets, blow over the Adriatic Sea (Cavaleri and Bertotti, 2004; Barbariol et al., 2021). Second, southerly winds blow over the Ionian and Tyrrhenian Seas, namely, the Sirocco and Libeccio winds (Zecchetto and De Biasio, 2007). During spring and autumn, the Sirocco winds blow south-easterly (SE) and are channelled into the Adriatic Sea, whereas during winter, the Libeccio winds blow south-westerly (SW).

In the western MS (WMS), the cold, dry Mistral winds blows northerly or north-westerly over the French and north-eastern Spanish coasts (Pallares et al., 2014; Barbariol et al., 2021), extending over the Balearic, Sardinian and Tyrrhenian Seas. This wind jet is stronger during the winter than in other seasons. Additionally, the Levanter and Vendaval winds blow over the Alboran Sea in the most western part of the MS basin. The Vendaval winds blow south-westerly during the autumn and spring seasons, whereas the Levanter winds blow north-easterly year-round but are much stronger in winter than in other seasons (Lionello and Sanna, 2005).

Therefore, the MS wave climate is significantly conditioned by these wind regimes.

2.2. Bathymetric and coastline data

The ETOPO1 gridded bathymetric data (Amante and Eakins, 2009), with a spatial resolution of 1 arc-minute, were applied as the depth-boundary conditions in the MS wave model. Fig. 2 shows the basin bathymetry and the domain of the study area. Moreover, the full-resolution coastlines from the Global Self-consistent Hierarchical High-resolution Shoreline dataset (GSHHS) (Wessel and Smith, 1996) were employed in this study.

2.3. Wind field forcing

The high-resolution wind fields used to force the MS wave model were produced in the framework of the European project titled 'Uncertainties in Ensembles of Regional Re-Analysis' (UERRA). The 3D-VAR UERRA system of the ECMWF is based on the HARMONIE data assimilation system, which was developed and used within the HIRLAM and ALADIN models (Ridal et al., 2017). The UERRA system has been implemented and optimized for the European area covering the MS with a horizontal resolution of 11 km and 65 vertical levels, with higher resolutions at lower altitudes. The system uses data from global reanalyses as lateral boundary conditions, including ERA40 data (Uppala et al., 2005) for the 1961–1978 period and ERA-interim data for the 1979–2019 period. In the UERRA system, near-surface wind fields are downscaled at a horizontal resolution of 5.5 km from the 3D-Var reanalysis performed at 11 km with the UERRA-HARMONIE-v1 system and the ALADIN model. Accordingly, we employed the 6-h downscaled high-resolution (5.5-km) wind fields, known as the UERRA-MESCAN-SURFEX data, as the forcing fields.

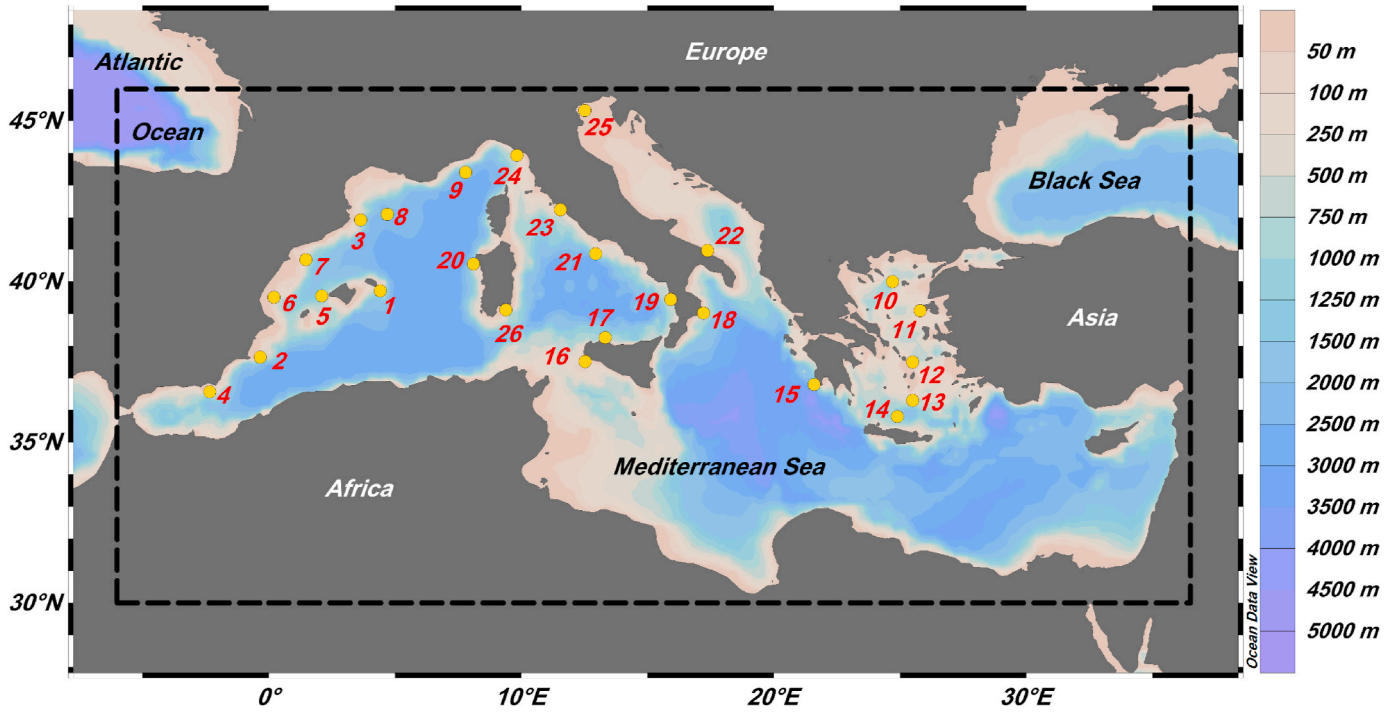

Fig. 2. Study area showing the model domain (the dashed rectangle), bathymetry and the locations of the wave buoys are shown in yellow circles and numbered in red.

2.4. Wave observations

2.4.1. Moored buoy observations

In this study, wave data measured at 26 offshore moored buoys were obtained from the quality-controlled MS In-Situ Near Real Time Observations product provided by the Copernicus Marine Environment Monitoring Service (CMEMS). Deep-water wave buoys with measurement records spanning more than two years were selected; see Fig. 2 for the specific locations of the buoys. Approximately 60% of buoys had recorded measurements for more than five years. The buoys are managed and maintained by a variety of agencies: the Spanish Port Authority (Puertos del Estado) REDEXT, the Italian buoy network RON (Rete Ondametrica Nazionale), Météo-France offshore French buoys, and the Poseidon Greek buoy network of the Hellenic Centre for Marine Research (HCMR). These offshore moored buoys provide H_s, mean wave period (T_{m02}), and mean wave direction (θ_m) measurements with varying, network-dependent temporal resolutions. Notably, buoy numbers 8 and 9 in Fig. 2, which correspond to the French offshore buoys with codes 61002 and 61001, respectively, do not provide measurements for either the mean period or the mean wave direction.

2.4.1. Altimeter dataset

The recent altimeter database of the Sea State Climate Change Initiative (SSCCI) (Dodet et al., 2020), provided by the European Space Agency (ESA), was used in this study. The first version of the SSCCI provided altimeter-recorded H_s data from multiple missions covering the period from 1991 to 2018. Ten platforms are included in the SSCCI database, namely, ERS-1 (1991–1996), ERS-2 (1995–2011), Topex-Poseidon (1992–2005), Geosat Follow On (GFO) (2000–2008), Jason-1 (2002–2013), Jason-2 (2008–2018), Jason-3 (2016–2018), Cryosat-2 (2010–2018), Envisat (2002–2012) and Saral (2013–2018). Each mission was quality-controlled and calibrated using data from moored buoys. Additionally, cross-calibrations were conducted among the different platforms (Stopa et al., 2019). The level-2 pre-processed (L2P) product in this database is an along-track, denoised and recalibrated altimeter-measured H_s product with a spatial footprint resolution of 7 km along the satellite track (Piollé et al., 2020; Dodet et al., 2020). This product was used in the current study for the calibration of the MS wave model and the validation of the MS wave hindcast. The L2P product includes H_s data with corresponding quality-flag values. Throughout the current study, only H_s data with a quality flag value of 3, meaning good and useable measurements, were used.

3. MS wave model setup, calibration, and hindcast production

This section describes the setup and calibration procedure of the MS wave model as well as the production of the MS wave hindcast dataset.

3.1. MS wave model setup

The MS wave model is based on the spectral wind wave model WW3 version 6.07. The WW3 model is a third-generation wave model that spatially and temporally integrates the spectral action equation to allow numerical modelling of wind-driven wave processes such as wave generation, propagation, and dissipation. The MS wave model domain covers the basin area between 6° W and 36.30°E and between 30° and 46° N, with a spatial resolution of 0.1° in longitude and latitude (Fig. 2). The wave spectral domain is discretized into 24 directions and 29 frequencies nonlinearly distributed from 0.05 Hz to 0.721 Hz with a frequency increment factor of 1.1. The bathymetry, land–sea mask, and obstruction grids were generated using the grid-generation software developed for WW3 (Chawla and Tolman, 2008). Obstruction grids were generated to reduce the energy fluxes in the x and y directions resulting from islands smaller than the spatial resolution of the MS wave model. WW3 requests the definition of four time steps, namely, the maximum overall global time step (Δt_g), the maximum CFL time step ($\Delta t_{x\text{-}y}$, used for spatial propagation), the refraction time step ($\Delta t_{k\text{-}\theta}$, used for spectral propagation) and the minimum source term time step (Δt_{min}). These time steps were set to 1800 s, 600 s, 900 s and 10 s, respectively, with the condition that the maximum $\Delta t_{x\text{-}y}$ value of the lowest-frequency waves must satisfy the CFL criterion.

The physical processes of wave generation, propagation, and

dissipation are parameterized in WW3. Following Stopa et al. (2016), we implemented the ST4 parameterization package developed by Ardhuin et al. (2010) for wind input and dissipation (see WW3DG, 2019). Moreover, Ardhuin et al. (2010) recommended the source-term TEST405 (T405) parameterization scheme of ST4 for wave modelling in regions characterized by short fetches such as those present in the MS and its sub-basins (Fig. 1). They stated that the T405 parameterization is preferred in the MS due to its superior performance for younger wind seas. Accordingly, in this study, we employed the T405 parameterization scheme and applied the default values for all parameters, except the non-dimensional wind wave growth parameter ($\beta_{\max}$), which we utilized to calibrate the model as described in the following subsections.

The Discrete Interaction Approximation (DIA) of Hasselmann et al. (1985) was used to model nonlinear wave−wave interactions. Dissipation due to bed friction was included using the SHOWEX formulation of Ardhuin et al. (2003). Moreover, shallow-water-depth breaking was adopted following the method described by Battjes and Janssen (1978), including the application of the Miche-style water limiter for maximum energy. Following Perez et al. (2017) and Alday et al. (2021), the reflection from shoreline and subgrid features was set to 0.05. Furthermore, the Ultimate Quickest third-order propagation scheme was implemented along with the garden-sprinkler-effect reduction scheme proposed by Tolman (2002).

3.2. MS model calibration

The source term parameterization of Ardhuin et al. (2010) includes wind input and energy dissipation source terms based on the formulation of Janssen (1991). It is written as a function of the wave action $N(k, \theta)$ for each wave number (k) and direction (θ) as follows:

$$S_{in}(k,\theta) = \frac{\rho_a}{\rho_w}\frac{\beta_{max}}{\kappa^2} e^Z Z^4 \left(\frac{u_*}{C} + z_\alpha\right)^2 cos^{Pin}(\theta - \theta_u)\sigma N(k,\theta) + S_{out}(k,\theta) \quad (1)$$

where $\beta_{\max}$ is a non-dimensional wind wave growth parameter, ρ_w and ρ_a are the densities of water and the atmosphere, respectively, κ is the von Karman constant, Z is the parameterized sea surface roughness, P_{in} is a constant that controls the directional distribution of S_{in}, u^* is the wind friction velocity, and z_α is the wave age tuning parameter. Moreover, C is the wave celerity, σ is the wave frequency, S_{out} is the dissipation source term, and θ_u and θ are the wind and wave directions, respectively.

Following the calibration guidance proposed by Stopa (2018), we adjusted the $\beta_{\max}$ parameter to minimize the overall H_s bias and the root mean square error between the wave model results and the altimeter data. Here, $\beta_{\max}$ was optimized by minimizing the differences among the 10th, 50th, 99th and 99.5th percentiles of the H_s distribution from both the altimeter data and model results, thus fulfilling the following condition:

$$-0.1\ m < \ P(10,50,99,99.5)_{WW3,Hs} - P(10,50,99,99.5)_{\ ALT,Hs} < 0.1\ m \quad (2)$$

Therefore, the different energetic sea states of the H_s probability distribution should match between the model and altimeter observations. The calibration was carried out using a 1-year hindcast to avoid overfitting to a particular season or month (Stopa, 2018; Alday et al., 2021; Soran et al., 2022). The year 2011 was selected for the calibration of the model, as a large amount of altimeter data were available in this year and because it was one of the stormiest years on record (Hanafin et al., 2012; Ardhuin et al., 2019; Alday et al., 2021). During 2011, five altimeter platforms were available: ERS-2, Jason-1, Jason-2, Envisat, and Cryosat-2.

Accordingly, the WW3 model was run four times for the 2011 wave hindcast using tested values (1.55, 1.80, 2.25, and 2.40) of the wind-wave growth parameter $\beta_{\max}$. Notably, the $\beta_{\max}$ value of 1.55 is used as the default value for this parameter in WW3 when employing the T405 parameterization (WW3DG, 2019; Ardhuin et al., 2010). From the altimeter data, the recalibrated and denoised H_s values in 2011 were employed as the benchmark. First, the modelled H_s values were co-located over the satellite tracks by applying linear temporal interpolation and a bilinear spatial interpolation methods to match the scattered positions of the altimeter observations along the satellite tracks. Then, H_s data pairs from WW3 and altimeters were aggregated in $0.25^\circ \times 0.25^\circ$ grid cells to calculate several error metrics (e.g., the bias, scatter index, and root mean square error) for each cell. Altimeters typically perform poorly at distances up to 20 km from coasts (Passaro et al., 2015; Ardhuin et al., 2019) due to the inhomogeneity of coastal backscattering in satellite footprints affecting the retrievals; this effect is particularly notable within 20 km from coastlines (Dodet et al., 2020). Accordingly, a quality flag was applied such that only altimeter data recorded at distances from coasts greater than 20 km were considered.

Standard error metrics were used for the MS wave model calibration and, later, for the MS wave hindcast validation, including the bias, root mean square error (RMSE), scatter index (SI) and Pearson coefficient of correlation (R); the equations of these terms are given as follows:

$$Bias = \frac{1}{n}\sum(X_{mod} - X_{obs}) \quad (3)$$

$$RMSE = \sqrt{\frac{1}{n}\ (X_{mod} - X_{obs})^2} \quad (4)$$

$$SI = \sqrt{\frac{\sum\left((X_{mod} - \overline{X_{mod}}) - (X_{obs} - \overline{X_{obs}})\right)^2}{\sum (X_{obs})^2}} \quad (5)$$

$$R = \frac{\sum(X_{mod} - \overline{X_{mod}})(X_{obs} - \overline{X_{obs}})}{\sqrt{\sum(X_{mod} - \overline{X_{mod}})^2}\sqrt{\sum(X_{obs} - \overline{X_{obs}})^2}} \quad (6)$$

where X_{mod} is the modelled wave parameter, X_{obs} is the wave parameter observed in the altimeter or buoy measurements, and n is the number of data pairs. The overbar represents the mean of all samples. The slope of the linear regression was also employed.

As mentioned above, this calibration procedure includes metric statistics for the four tested $\beta_{\max}$ values. Consequently, the different percentiles (10th, 50th, 99th and 99.5th) of the H_s distributions were computed for both the modelled and altimeter-recorded data. To optimally determine the $\beta_{\max}$ parameter value, the previously mentioned percentiles were computed for the modelled H_s values co-located along the satellite tracks; then, the H_s residuals (i.e., $H_{s,\ WW3}$ - $H_{s,\ ALT}$) were calculated for the different percentiles to satisfy the condition given by Eq. (2). Accordingly, when comparing the H_s residuals against the tested $\beta_{\max}$ values, the optimum $\beta_{\max}$ value was the value resulting in negligible H_s residuals among the different percentiles.

As shown in Fig. 3, the results indicate an optimum $\beta_{\max}$ value of 2.25; this value produced the minimum residual in the hindcast H_s distribution evaluated at several percentiles. This means that the 1-year hindcast produced with a $\beta_{\max}$ value of 2.25 best matched the different percentiles of the H_s distribution between the modelled and altimeter-recorded data, with H_s residuals within ±0.1 m. The values of the different error metrics derived for the four tested $\beta_{\max}$ values are listed in Table 1. Fig. A.1, in Appendix A, shows two scatter plots of the H_s pairs obtained from the model data and altimeter observations recorded in 2011 using the default value of $\beta_{\max} = 1.55$ as well as the optimum value of $\beta_{\max} = 2.25$, which resulted in the minimum bias value and optimal error metrics. Similar to the wave-hindcasting results obtained in the MS by Barbariol et al. (2021), Fig. A.1 and Table 1 show that underestimated modelled H_s values with an overall bias of −0.148 m and a linear slope of 0.848 were derived when the default $\beta_{\max}$ value of 1.55 was used in WW3.

3.3. MS wave hindcast production

After calibration, the MS wave model was run over the 1961–2018

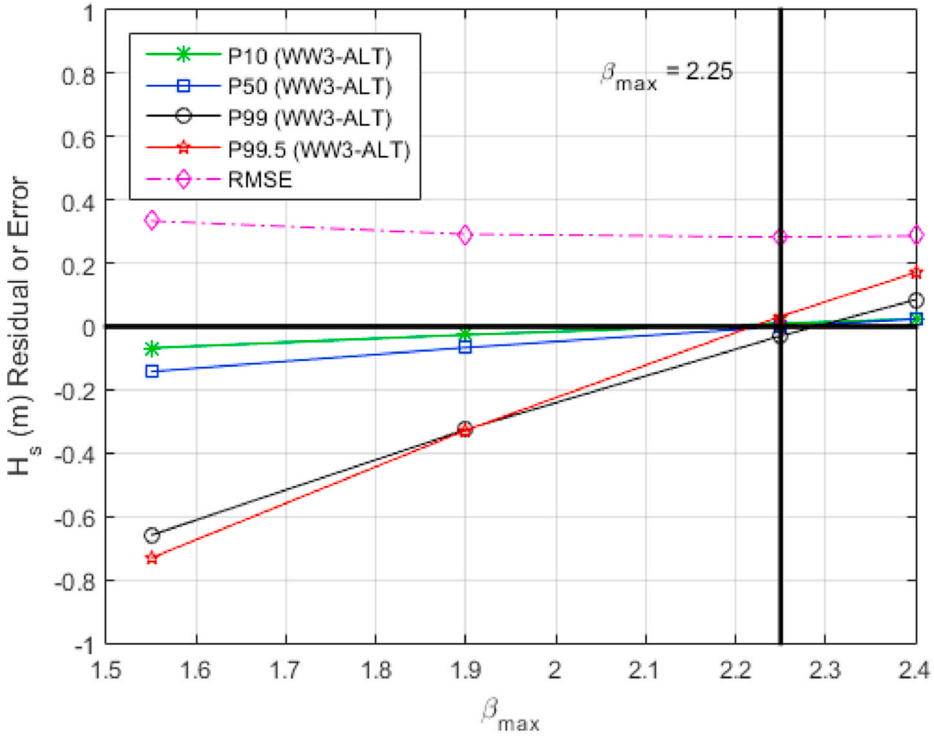

Fig. 3. Optimization of the β_{max} parameter in WW3 using model results and altimeter observations of H_s for the year 2011. The green, blue, black and red lines are, respectively, the 10th, 50th, 99th and 99.5th percentiles of H_s residual, i.e., the H_s from WW3 minus the H_s from altimeter. The magenta dashed line represents the root mean square error. The optimum β_{max} value is specified by the vertical black line.

Table 1
Error metrics for the tested values of β_{max} for model calibration based on a 1-year hindcast. The calibration is carried out using altimeter H_s data of the year 2011. The β_{max} in bold is the final value used to force the model for the development of the MS hindcast.

β_{max}	Bias (m)	RMSE (m)	SI	R	Lin. Slope
1.55	−0.149	0.331	0.196	0.922	0.848
1.90	−0.072	0.292	0.191	0.923	0.9145
2.25	**−0.005**	**0.284**	**0.193**	**0.922**	**0.973**
2.40	0.020	0.290	0.196	0.922	0.996

period. The MS wave hindcast consists of hourly sea-state parameters of the 2D wave spectrum outputted at each grid point for 58 years. These sea-state parameters include the H_s, mean wave periods (T_{m01} and T_{m02}), θ_m, directional spreading (σ_θ), spectral peak frequency (f_p), and wave energy flux (EC_g). Additionally, the hourly parameters of the partitioned 2D wave spectrum in one sea and five swell partitions (Vincent and Soille, 1991; Hanson and Phillips, 2001), including H_s, f_p, θ_m, and σ_θ, were stored at each grid point. Moreover, three hourly time series of the 2D wave spectrum were stored along the MS coastal areas at water depths exceeding 200 m, with a spacing of 0.20°. Such long-time-series directional spectra are useful for investigating multimodal wave climate variabilities and as boundary conditions for modelling the nearshore transformation of waves in coastal engineering applications, offshore engineering, and maritime navigation; as reconstructing the wave spectra from wave partitions is still challenging (Albuquerque et al., 2021).

4. Performance of the MS wave hindcast

The MS hindcast dataset was validated against both in situ buoy records and altimeter observations. The data validation process is described in this section.

4.1. Validation with buoy measurements

The model-derived sea-state parameters, including H_s, T_m, and θ_m, were compared with the corresponding wave parameters measured by 26 offshore buoys available in the MS (Fig. 2).

The standard error metrics (bias, RMSE, SI, and R, as previously used for the model calibration described in Section 3.2) were utilized to quantify the errors of the scalar wave parameters, i.e., H_s and T_m. Nonetheless, the error in the θ_m estimation was evaluated using the normalized bias of directions (NBI_θ) and the normalized root mean square error ($NRMSE_\theta$), employing a 2π radiant angle for normalization (Mentaschi et al., 2015; Vousdoukas et al., 2017; Umesh and Behera, 2020); these terms can be expressed as follows:

$$NBI_\theta = \frac{\sum mod_{-\pi,\pi}(\theta_{mod} - \theta_{obs})}{2\pi\, n} \tag{7}$$

$$NRMSE_\theta = \frac{\sqrt{\frac{1}{n}\Sigma\left(mod_{-\pi,\pi}(\theta_{mod} - \theta_{obs})\right)^2}}{2\pi} \tag{8}$$

where θ_{mod} and θ_{obs} are the modelled and observed mean wave directions, respectively. Furthermore, the modulo operator $mod_{-\pi,\pi}$ indicates that if (θ_{mod} - θ_{obs}) < -π, a 2π angle is added to the difference, while if (θ_{mod} - θ_{obs}) > π, a 2π angle is subtracted from the difference (Mentaschi et al., 2015; Umesh and Behera, 2020). Additionally, other error metrics were used to compare the results of the current study with those of previous studies. These metrics include the normalized root mean square error (HH index) introduced by Hanna and Heinold (1985) and the index of agreement (d) introduced by Willmott et al. (1985); these metrics are expressed as follows:

$$HH = \sqrt{\frac{\sum (X_{mod} - X_{obs})^2}{\sum (X_{mod} * X_{obs})}} \tag{9}$$

$$d = 1 - \frac{\sum (X_{mod} - X_{obs})^2}{\sum \left(|(X_{mod} - \overline{X_{obs}})| + |(X_{obs} - \overline{X_{obs}})|\right)^2} \quad (10)$$

The scatter plots shown in Fig. A.2 were constructed to compare the modelled and measured H_s and T_m values for the whole set of buoys employed in the current study. The values of the overall error metrics are summarized in Table 2. We found negligible positive biases, an almost one-one linear regression slope, and RMSEs of 0.323 m and 0.733 s for the H_s and T_m results, respectively. Thus, strong agreement between the calibrated model results and in situ observations was achieved. Similar scatter plots are shown in Fig. A.3 when using the default $\beta_{\max}$ value, revealing an underestimation of both H_s and T_m with negative biases of −0.06 m and −0.112 s, respectively. Additionally, the linear slope is less than 1 for both wave parameters.

In general, the statistics obtained based on the validation of the hindcast against buoy records were better than those achieved in previous studies performed in the MS (e.g., Mentaschi et al., 2015). The HH values of H_s were 0.25 and 0.34 in the current study and in Mentaschi et al. (2015), respectively. Both wave datasets showed similar T_m results, with an HH value of 0.18. Regarding the wave direction (θ_m), the current hindcast resulted in an NBI_θ of 0.216% (see Table 2), corresponding to a bias equal to 0.778°, i.e., less than 1°. This represents a significant improvement in the θ_m estimation compared to the results of other hindcasts performed in the basin, such as that of Mentaschi et al. (2015), which revealed a bias of 3.6°. This may be attributed to the high spatial resolution of the wind fields used to force the wave model resulting in an improved ability to represent local atmospheric features and wind directions accurately in this semi-enclosed basin with complex surrounding orography.

The performance of the model at each buoy for each wave parameter and the error metrics considered herein are summarized in Table A1. This same information is also provided graphically in Fig. 4 in the form of Taylor diagrams (Taylor, 2001) for the H_s and T_m parameters. In the Taylor diagrams, the standard deviation of the model output is normalized by dividing it by that of the buoy measurements. In these diagrams, the shorter the distance to the point marked as 'Buoys' is, the better the model performance is. Despite the general trend in which the MS hindcast yielded better H_s results than T_m results, T_m was estimated robustly and compared quite well with the in situ observations, showing a negligible bias and a low RMSE (see Table 2).

In addition, as an example, the time series of the modelled wave parameters and those measured by the Cabo de Palos offshore buoy (61417) in the WMS are shown in Fig. 5, indicating that the MS hindcast can correctly represent the temporal evolution of H_s, T_m, and θ_m, also capturing the severe storm that occurred in November 2012.

4.2. Validation with altimeter data

Denoised and recalibrated H_s data from the altimeter database (Dodet et al., 2020), available for the period from 1991 to 2018, were used to validate the MS wave hindcast by applying the procedure described in Section 3.2. Thus, the validation was carried out for the 27-year period in which data were available ($>6.58 \times 10^6$ co-located points in the basin). Fig. A.4 shows the scatter plot of H_s pairs from the MS wave hindcast and altimeter series for the 1991–2018 period. The MS wave hindcast performance resulted in a bias of 0.022 m and RMSE, SI, correlation coefficient and linear slope values of 0.300 m, 0.200, 0.928 and 0.990, respectively. Moreover, the quantile−quantile plot of the co-located modelled H_s along the satellite tracks and the altimeter data shown in Fig. A.4 indicates strong agreement between the two datasets with regards to the different H_s percentiles, ranging from the lower percentiles ($H_{s,10}$) corresponding with relatively calm conditions to the larger percentiles ($H_{s,99.9}$) corresponding with extreme values. It is worth pointing out that using the default settings of the WW3 model, without optimizing $\beta_{\max}$, resulted in an underestimation of the modelled H_s values in comparison with altimeter data with a bias and a linear slope of −0.126 m and 0.86, respectively, see Fig. A.5. A clear underestimation of H_s takes place all the way between the mean conditions ($H_{s,50}$) and extremes ($H_{s,99.9}$) as shown in the quantile-quantile plot of Fig. A.5.

Similar to the hindcast performance against buoy measurements, the validation results against the altimeter data revealed an improvement in the H_s error metrics compared to those reported in previous studies in the MS (Donatini et al., 2015; Barbariol et al., 2021; Lira-Loarca et al., 2022; Toomey et al., 2022). As indicated above, here, we obtained smaller RMSE and SI values in comparison to the results of Donatini et al. (2015), who revealed RMSE and SI values of 0.34 m and 0.25, respectively. Moreover, the results obtained in the current study indicate optimal values of both the bias and linear slope compared to those achieved by Barbariol et al. (2021), with a negative bias of −0.12 m and a slope of 0.87. Furthermore, the current study shows an index of agreement (d) of 0.96, higher than that obtained by Lira-Loarca et al. (2022) (0.65) for the whole MS. Additionally, the current study improves the estimation of the H_s higher quantiles providing reliable results all the way to H_s reaching 6 m (see Fig. A.4), whereas the quantile-quantile analysis performed by Toomey et al. (2022) revealed an underestimation of wave heights for the domain of H_s exceeding 4.8 m.

Fig. 6 shows the spatial distributions of the error metric statistics describing the performance of the MS wave hindcast against the altimeter data during the 1991–2018 period, showing overall good agreement. Negligible biases were obtained in most areas of the basin. Slightly negative values were obtained in the eastern and central MS areas, whereas slightly positive biases were encountered in the western MS, especially in the gulf of Lyon (northern Sardinian Sea) and the most western part of the Alboran Sea. The RMSEs were approximately 0.30 m in most regions of the MS. As observed for the bias results, relatively large RMSE values were found in the Alboran Sea and the offshore French coasts compared to the rest of the MS basin. Correlation values larger than 0.9 were obtained in the MS basin. Additionally, the scatter index showed an almost consistent value of 0.20 in the entire MS basin. Similar to Fig. 6, Fig. A.6 shows the spatial distribution of the error metrics when using the default value of $\beta_{\max}$ revealing a negative bias in the whole MS basin and larger RMSE values up to 0.5 m in a large portion of the basin including the Sardinian Sea, Ionian Sea, and the Levantine Sea.

The MS wave hindcast performance in the different sub-basins revealed strong agreement between the modelled and satellite-derived H_s data. This agreement can be seen in Fig. A.7 by comparing the histogram of the modelled H_s against the corresponding one from the altimeter observations representing the MS basin (the Panel Mediterranean), as well as the different sub-basins (the Alboran-Balearic, Sardinian, Adriatic, Tyrrhenian, Ionian, Aegean and Levantine Panels). Strong agreement was obtained for $H_s > 1$ m, with Pearson correlations exceeding 0.91. Furthermore, the upper tails of the distributions (sea states characterized by $H_s > 2$ m) strongly matched. Similarly, the central regimes (sea states characterized by $H_s = 1$–2 m) and lower tails of the distribution (sea states characterized by $H_s < 1$ m) showed good

Table 2
Validation results, in terms of error metrics, of the MS hindcast against in-situ wave buoys data of the significant wave height, mean period and mean direction.

H_s					T_m					θ_m	
Bias (m)	RMSE (m)	SI	R	Lin. Slope	Bias (s)	RMSE (s)	SI	R	Lin. Slope	NBI_θ (%)	$NRMSE_\theta$
0.082	0.323	0.25	0.915	1.054	0.041	0.733	0.188	0.714	1.002	0.216	0.1285

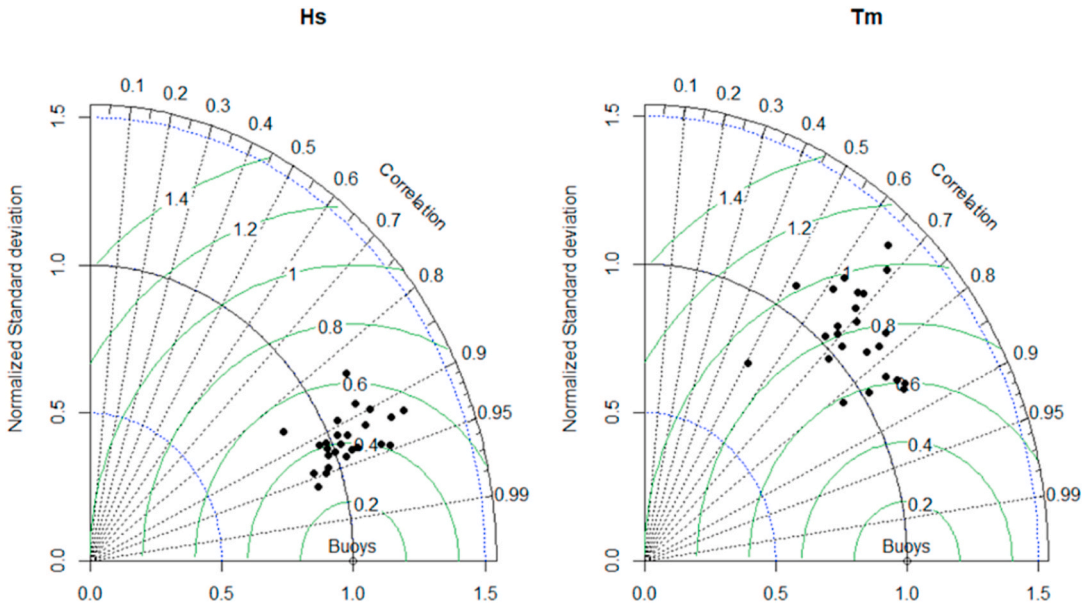

Fig. 4. Taylor diagrams (Taylor, 2001) displaying the performance of the MS hindcast against buoys for H_s and the T_m. Each point represents one buoy. Shorter distances to the point marked as 'Buoys' indicate better validation results than larger ones. Blue and green circles refer to the normalized standard deviation and the RMSE, respectively, whereas the dashed straight lines correspond to the correlation coefficient values.

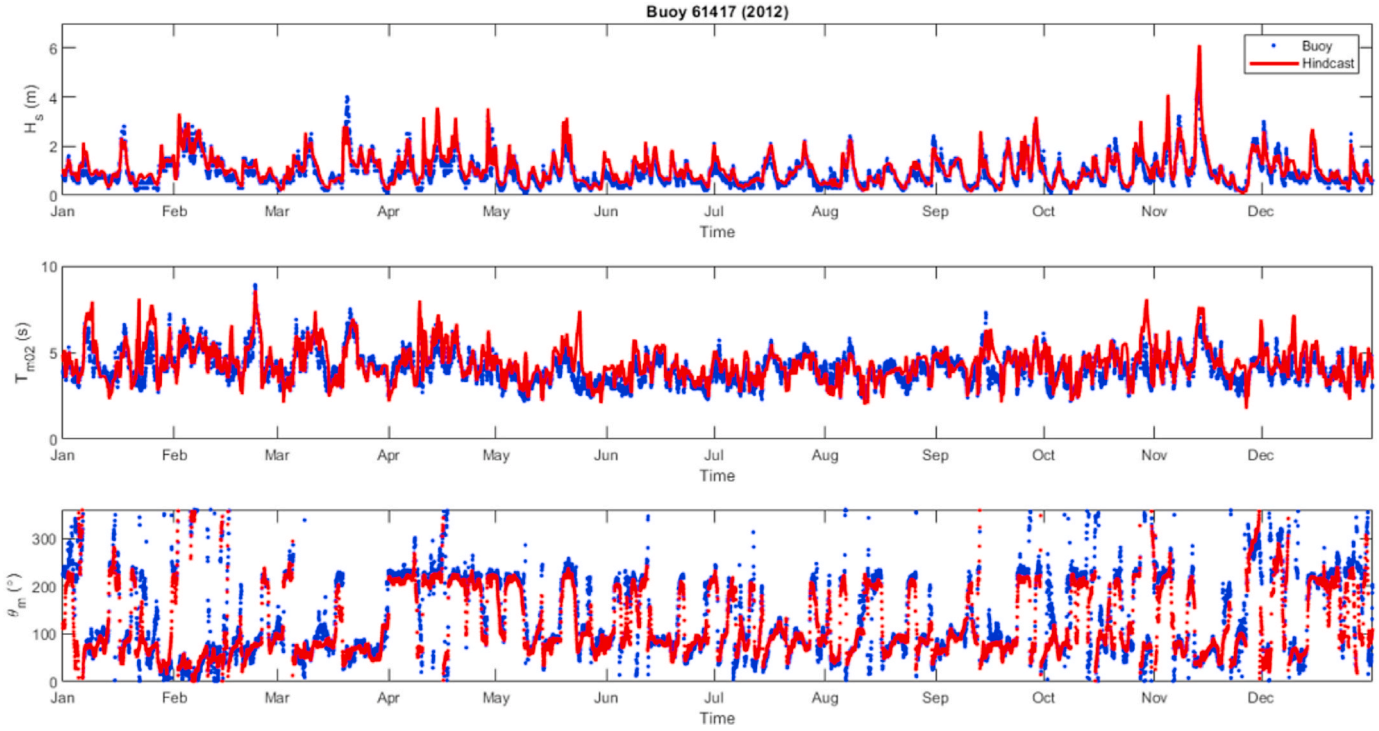

Fig. 5. Time series of the significant wave height (H_s), the mean period (T_{m02}) and the mean wave direction (θ_m) for the year 2012 at the location of Cabo de Palos buoy (61417). The buoy data is shown in blue dots, while the hindcast wave parameters from WW3 are displayed in red.

agreement, providing correlations larger than 0.98. Minor differences in the lower tails of the distributions were found in the narrow sub-basins with short fetches (the Adriatic and Aegean Seas). This may be attributed to the tendency of the model to underestimate wave growth on very short fetches (Mentaschi et al., 2015) or is perhaps a consequence the altimeter wave height measurements being unreliable below 0.75 m (Cavaleri et al., 2018; Dodet et al., 2020; Alday et al., 2021).

In general, the validation results obtained herein are amply suitable for the wave climate analysis and characterization addressed in the following section.

5. Mediterranean sea wave climate

This section addresses the characterization of the MS wave climatology. First, the predominance of sea and swell energies in the wave spectra across the MS basin are assessed. Second, the mean and extreme regimes of the MS basin are described. Third, the magnitude of the intra-annual variability is discussed. Next, the interannual variabilities in the

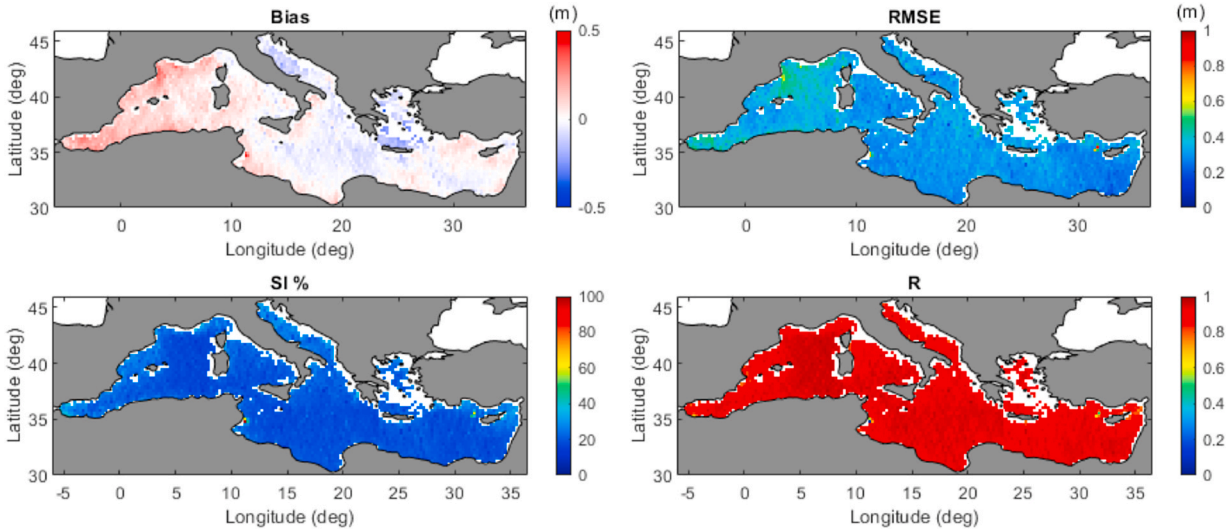

Fig. 6. Spatial distributions of the Bias (Bias panel), the RMSE (RMSE panel), the scatter index (SI % panel), and the correlation coefficient (R panel) in H_s using the optimum value of $\beta_{max} = 2.25$. The performance of the MS hindcast is evaluated using, as benchmark, the SSCCI altimeter data of H_s from 1991 to 2018.

MS wave climatology are correlated with large-scale atmospheric patterns. Then, the wave storminess characteristics are described. Finally, the long-term trends in intra-annual, interannual, and storminess variabilities are evaluated. The characterization is based on statistics of spectral parameters that describe the 2D wave spectrum and on existing wave systems analysed through the usage of spectral wind and swell partition parameters.

5.1. Wind seas and swells throughout the MS

The mean wind sea fraction (*WSF*) of the hourly wave spectra was calculated for the 1961–2018 period. In WW3, this term is estimated by partitioning the wave spectrum into different wave systems following the algorithm developed by Vincent and Soille (1991) and the methodology of Hanson and Phillips (2001), thereby identifying the wind sea energy portion of the wave spectrum. As described in Tracy et al. (2007), the *WSF* can be defined as follows:

$$WSF = \frac{E|_{U_p > C}}{E} \tag{11}$$

where E is the total spectral energy and $E|_{U_p>C}$ is the energy in the spectrum for which the projected wind speed U_p is larger than the local wave celerity C. The latter defines an area in the spectrum under the direct influence of the wind. U_p is given as follows (see WW3DG (2019)):

$$U_p = 1.7 * U_{10} \cos(\theta - \theta_u) \tag{12}$$

where U_{10} is the surface wind velocity at 10 m over the sea surface. In this study, the mean *WSF* is used as an indicator of the distribution of the hourly wind sea and swell energies in the MS basin (Fig. 7). In previous studies, the MS wave climate has been said to be driven mainly by regional winds, suggesting a predominance of local wind seas (Cavaleri et al., 2018). We found that in a large portion of the MS basin, the swell energy has a slight influence ($0.25 < WSF < 0.45$), thus confirming the notable presence of wind-sea energy in the hourly spectra. Notably, the Gulf of Lyon (in the northern Sardinian Sea) and the Alboran Sea in the WMS, the Adriatic Sea in the CMS, and the Aegean Sea in the EMS are characterized by larger wind sea fractions ($WSF > 0.65$) than the rest of the MS basin. In these sub-basins, the wind sea influence can be significant ($0.75 < WSF < 0.95$, see Fig. 7), or the wind sea can dominate ($0.95 < WSF < 1$, see Fig. 7), corresponding with the wave generation domains attributed to the wind systems that are active in these areas: the Mistral winds dominate in the Gulf of Lyon, the Vendaval and Levanter winds dominate in the Alboran Sea, the Bora and Sirocco winds dominate in the Adriatic Sea, and the Etesian winds dominate in the Aegean Sea (Fig. 1).

5.2. Mean and extreme wave climatology regimes in the MS

A characterization of the wave climatology in the MS basin and in each sub-basin was conducted for the 1961–2018 period by assessing the indicators of the mean regime (the 50th percentile), the extreme regime (the 99.5th percentile), and the maximum value. Henceforth, these

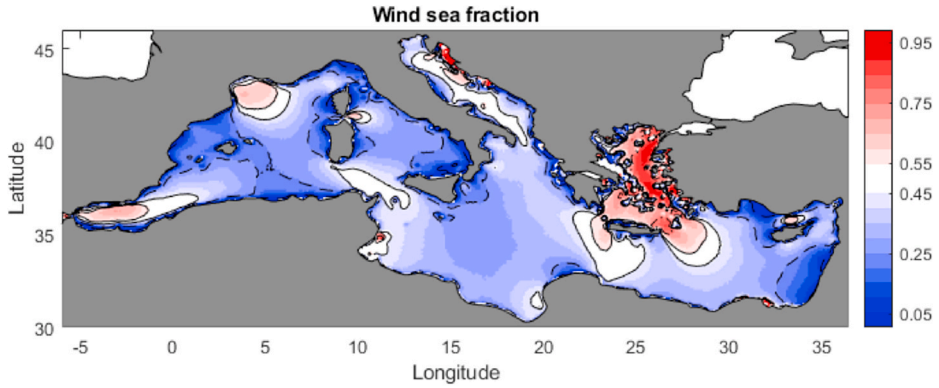

Fig. 7. The spatial distribution of the mean wind sea fraction (*WSF*) during the period 1961–2018 in the MS basin. The colour map represents *WSF*, with $WSF = 0$ for predominance of swell energy, and $WSF = 1$ for wind sea predominance in the wave spectra. $0 < WSF < 0.05$ for swell dominated; $0.05 < WSF < 0.25$ for significant swell influence; $0.25 < WSF < 0.45$ for slight swell influence; $0.45 < WSF < 0.55$ for neutral wind sea and swell influence; $0.55 < WSF < 0.75$ for slight wind sea influence; $0.75 < WSF < 0.95$ for significant wind sea influence; $0.95 < WSF < 1$ for wind sea dominated. The continuous contour line delimits $WSF = 0.45$ and $WSF = 0.55$, the dashed contour line delimits *WSF* of 0.05 and 0.25, and the point dashed line delimits *WSF* of 0.75 and 0.95.

terms are referred to as the median, threshold, and maximum values and are applied to the univariate H_s and T_m parameters. Fig. 8 shows the spatial distributions of these values ($H_{s,50}$, $T_{m,50}$, $H_{s,99.5}$, $T_{m,99.5}$, $H_{s,\ max}$, and $T_{m,\ max}$) in the MS basin. In summary, the spatially averaged median H_s and T_m values were $H_{s,50} = 1.1$ m and $T_{m,50} = 4.72$ s, respectively; the spatially averaged threshold H_s and T_m values were $H_{s,99.5} = 4.20$ m and $T_{m,99.5} = 8$ s, respectively; and those of the maximum H_s and T_m values were 8.94 m and 10.85 s, respectively. The spatially averaged values of these three indicators were conditioned by the extent of each sub-basin relative to the total MS area; as seen in Fig. 8, the spatial variability was significant.

For the mean conditions, $H_{s,50}$ shows values above 1.1 m in the MS basin except the Adriatic, Tyrrhenian, and Aegean Seas, where the $H_{s,50}$ values are <1 m. It is worth noting that the maximum $H_{s,50}$ values are encountered in the western MS, within the Sardinian Sea area, with values up to 1.50 m. Comparably, $T_{m,50}$ shows values of approximately 5 s in a large percentage of the MS basin, excluding the Adriatic and Aegean Seas, where $T_{m,50} < 4$ s. Then, the maximum $T_{m,50}$ values are found in the Sardinian Sea area, reaching 6 s.

Regarding extreme conditions, the threshold H_s values, $H_{s,99.5}$, ranged from 4 to 5 m in a large area of the MS basin, increased to 6 m in the Sardinian Sea, and showed relatively low values ($H_{s,99.5} < 4$ m) in the short-fetch sub-basins (the Adriatic and Aegean Seas). In contrast, the $T_{m,99.5}$ thresholds exhibited clear zoning, with periods up to 10 s observed in the Sardinian Sea, values of 8 s in the Ionian and Levantine Seas, and relatively low values ($T_{m,99.5} < 7$ s) in the Adriatic and Aegean Seas. The maximum wave conditions reveal that the maximum H_s value, $H_{s,max}$, occurred in the eastern Tyrrhenian Sea (near the south-western Italian coast), with a $H_{s,max}$ value > 10 m. The western MS (WMS), the Sardinian Sea, and the Ionian Sea of the central MS (CMS) exhibit slightly lower values ($H_{s,max}$ reaching 10 m). In the Levantine Sea, the $H_{s,\ max}$ values reached 9 m in the areas very far offshore. Regarding the maximum T_m, $T_{m,max}$, the spatial distribution of these values indicates the presence of waves with $T_{m,max}$ values ranging from 10 to 12 s in a large percentage of the MS basin, with the exception of the Adriatic and Aegean Seas, which are characterized by relatively short wave periods ($T_{m,max} = 8$–10 s). For more specific details on the spatial variabilities in the mean and extreme regime indicators, we refer the reader to Fig. 8.

Regarding the wave directionality in the MS, Fig. 9 displays the θ_m results in the basin during the 1961–2018 period. At the Levantine Sea in the EMS, the θ_m values range from the north to northwest direction. This result is attributed to the Etesian winds dominating that region. Moreover, the Adriatic Sea in the CMS is characterized by θ_m values ranging from the southwest direction along the longitudinal axis of this sub-basin because Sirocco winds are channelled in this area. The results also indicate the presence of northeast waves in the northern Sardinian Sea in the WMS, together with south-to-south-west waves in the Balearic Sea in the WMS due to the southwest Vendaval winds affecting this area. Consequently, bimodal wave climates are present along the north-eastern Spanish coasts, where double-peaked spectra are often observed (Sánchez-Arcilla et al., 2008; Elshinnawy et al., 2017). Accordingly, the MS hindcast properly captures such directional-variability features in this zone because of the high accuracy of the modelled wave directions resulting from the high-resolution wind forcing data employed. It is worth noting that the results also show that the θ_m direction indicates movement from the south in the Alboran Sea in the WMS. This zone of the south-eastern and southern Spanish coasts is characterized by sea states originating from both the south-eastern and south-western quadrants (Camus et al., 2011; Elshinnawy et al., 2017), leading to bimodal wave climates along these coasts of the Iberian Peninsula. Thus, the integral θ_m direction in this area is from the south, but it does not properly represent the different wave systems in

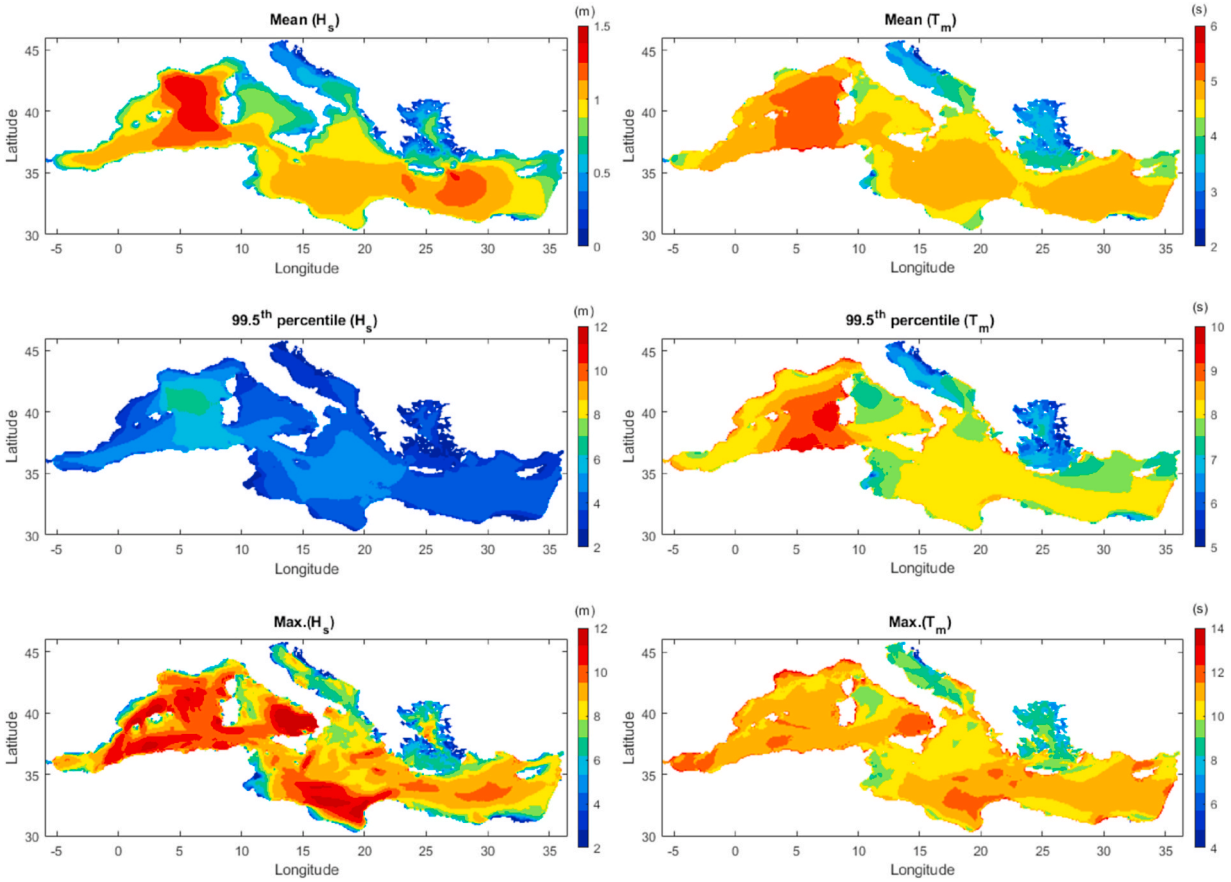

Fig. 8. The spatial distributions of the mean, the 99.5th percentile, and the maximum values of H_s (meters) and T_m (seconds) in the period 1961–2018.

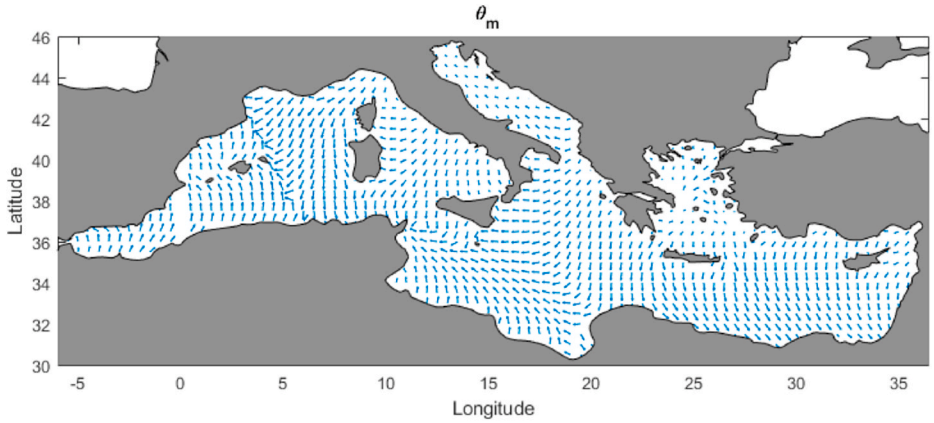

Fig. 9. The mean hourly wave direction, θ_m, in the MS basin during the 1961–2018 period. The arrows represent the direction to where the waves are going, with the length of the arrows directly proportional to the value of $H_{s,50}$.

the area. Accordingly, detailed analyses of the different wave families from the wave partitions of the directional wave spectra are required to better understand such directional variability in this zone. Moreover, the characterization of the crossing, opposing and following seas in the MS basin should be addressed in the future. Such a study is mandatory because sea crossings often poses navigation problems for ships.

5.3. Wave climate intra-annual variability in the MS

The monthly mean wave climatology of the H_s results during the 1961–2018 period is shown in Fig. 10. $H^*_{s,50}$ was estimated as a single indicator representing the 50th percentile of the probability density function (PDF) of a particular month (e.g., all January months) during the 1961–2018 period. The most energetic wave heights were found to occur during the winter months (December–March), with $H^*_{s,50}$ values reaching 1.8 m in the Sardinian Sea due to the influence of the strong Mistral winds blowing during the winter season from the French inland region. In contrast, the highest waves occurred during the summer months in the Levantine Sea (mainly south of Crete) with $H^*_{s,50}$ values reaching 1.5 m. These waves are the result of the strong Etesian winds

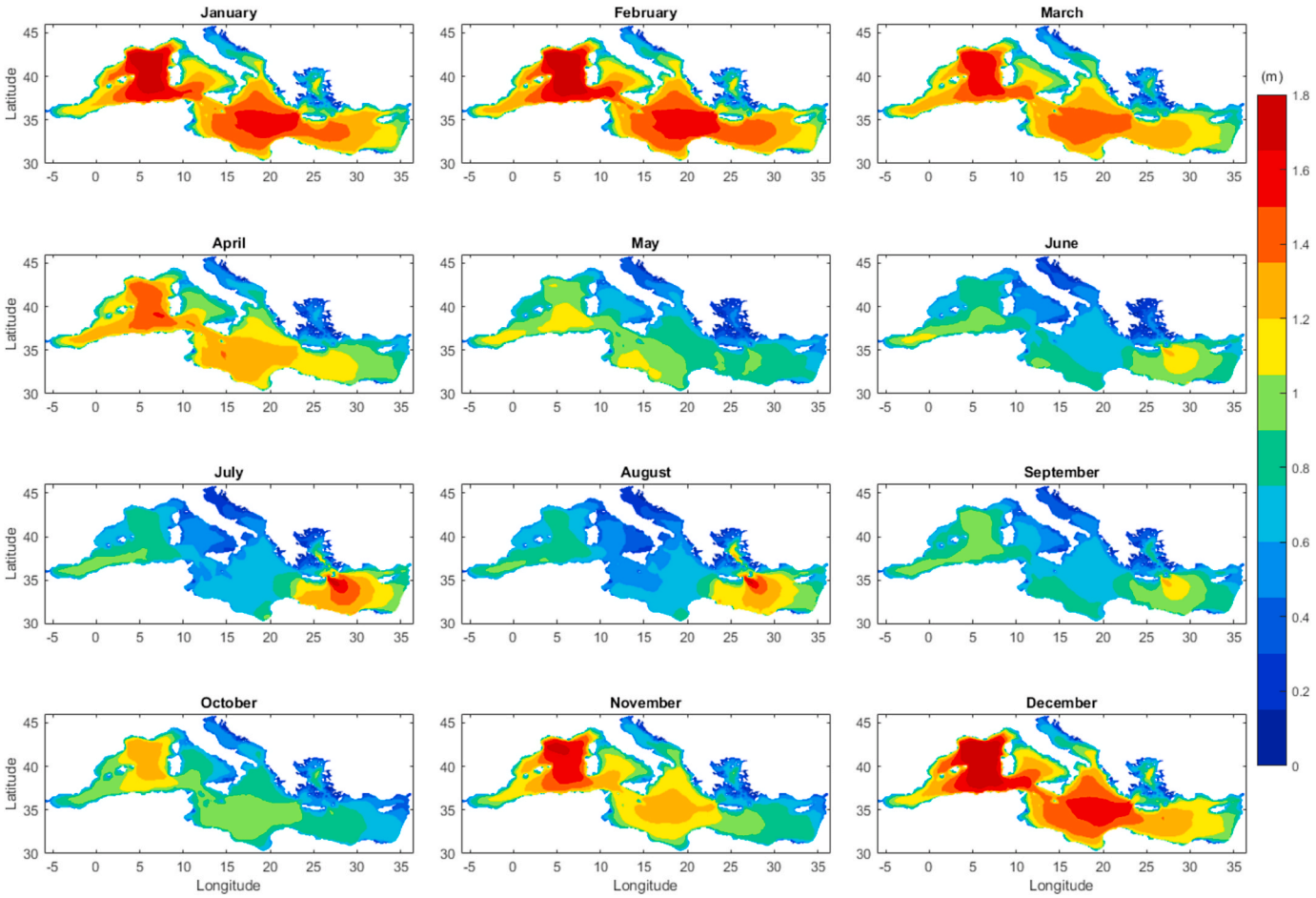

Fig. 10. $H^*_{s,50}$ as a representative indicator of the monthly mean wave climatology during the period from 1961 to 2018.

dominating the region in summer. Consequently, the spatial distribution of $H^*_{s,50}$ oscillated longitudinally between the summer and winter seasons, with the months of April and November sharing a very similar spatial pattern. The months of May and October also shared quite similar spatial distributions, with wave heights reaching 1 m in the MS basin. Additionally, similar $H^*_{s,50}$ distributions were also encountered during June and September. In summary, the Sardinian Sea exhibited the highest $H^*_{s,50}$ values throughout the year except in the summer season.

The monthly extreme wave height, $H^*_{s,99.5}$, was also estimated as a single indicator representing the 99.5th percentile of the PDF in a particular month during the 1961–2018 period. The results displayed in Fig. 11 show that the largest $H^*_{s,99.5}$ values consistently occur in the Sardinian Sea throughout the year. In this zone, the $H^*_{s,99.5}$ values reach 5.5–6 m during the November–March period, 4.5 m in April and October, and 4 m during the summer season. It is worth noting that the spatial distribution of the highest waves encountered in the MS differs between the mean and extreme conditions. In the Ionian Sea of the CMS, $H^*_{s,99.5}$ exhibits values up to 4.5 m and 2 m during the winter and summer seasons, respectively. In the Tyrrhenian Sea, the same spatial pattern as that observed in the CMS is seen because of the south-western Libeccio winds being stronger in the winter season than in the other seasons. Moreover, in the EMS, mainly in the Aegean Sea and Levantine Sea, the $H^*_{s,99.5}$ value reaches 4 m during the winter and 3 m in the summer because of the north-westerly Etesian winds dominating this area. The southern part of the Adriatic Sea is characterized by $H^*_{s,99.5}$ values reaching 3.5 m during the winter because of the south-easterly Sirocco winds. Furthermore, smaller $H^*_{s,99.5}$ values (reaching 2 m) occurred during the summer than in the other seasons in this sub-basin.

The results indicate clear seasonal variability in the directional wave climate in the MS basin with different patterns among the EMS, CMS, and WMS regions. The seasonal anomaly of the mean hourly wave direction ($\Delta\theta_{ms}$) was calculated by obtaining the difference between the seasonal mean hourly wave direction θ_{ms} and the mean hourly wave direction θ_m during the 1961–2018 period. The $\Delta\theta_{ms}$ term can be used to characterize seasonal shifts in wave directionality and is shown in Fig. 12. The blue and red colour maps shown in Fig. 12 refer to the clockwise (CW) and counter-clockwise (CCW) turns of θ_{ms}, respectively. In the Levantine Sea in the EMS, θ_{ms} turned CW relative to θ_m, with $\Delta\theta_{ms}$ reaching 60° during winter, but turns CCW during the summer. At the Adriatic Sea in the CMS, θ_{ms} turns slightly CW during winter and autumn; however, it turns CCW during summer with $\Delta\theta_{ms}$ values up to 30° (see Fig. 12). The most-southern parts of the Ionian Sea in the CMS are characterized by CW- and CCW-turning of θ_{ms} during summer and winter, respectively, with $\Delta\theta_{ms}$ values up to 60°. In the Alboran Sea and Balearic Sea in the WMS, θ_{ms} also turns slightly CCW and CW during winter and summer, respectively, with anomalies reaching 20°. In the northern Sardinian Sea in the WMS, CW changes in θ_{ms} are found in winter and spring, while CCW changes take place during summer. Similarly, in the Tyrrhenian Sea in the WMS, θ_{ms} turns CW and CCW during winter and summer, respectively. During autumn, CW θ_{ms} turns reaching 20° occur in the whole MS basin except in the Levantine Sea, which exhibits CCW changes with anomalies up to 10°. Finally, smaller anomalies are found during springtime over the MS basin than during the rest of the year. These results show the opposing turning patterns of θ_{ms} in the MS between summer and winter, suggesting that θ_{ms} is an indicator that should not be averaged over relatively long periods in the MS. In summary, large $\Delta\theta_{ms}$ values (up to 60°) occur in the MS basin during winter and summer in the EMS and the most southern area of the

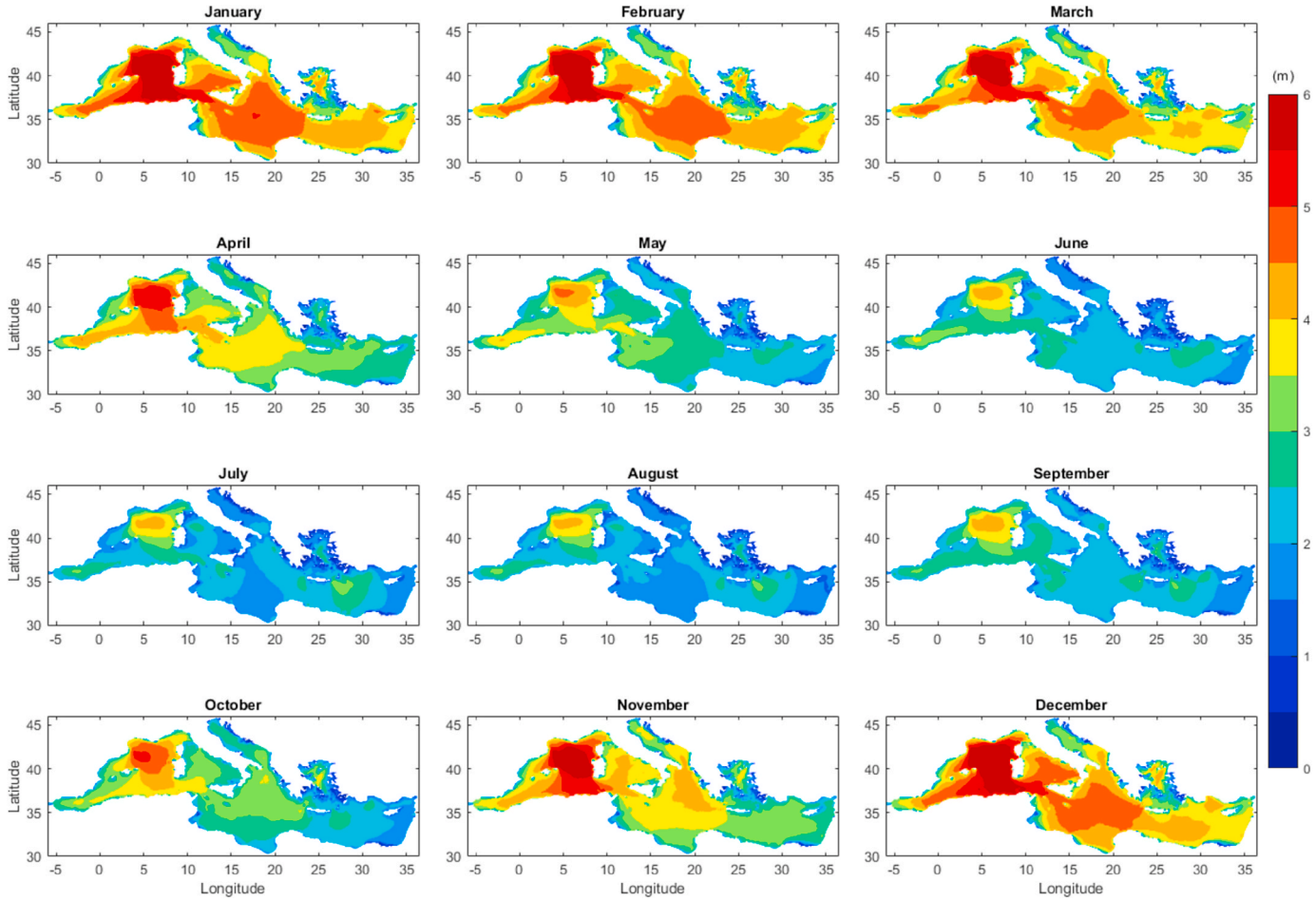

Fig. 11. $H^*_{s,99.5}$ as a representative indicator of the monthly extreme wave climatology during the period from 1961 to 2018.

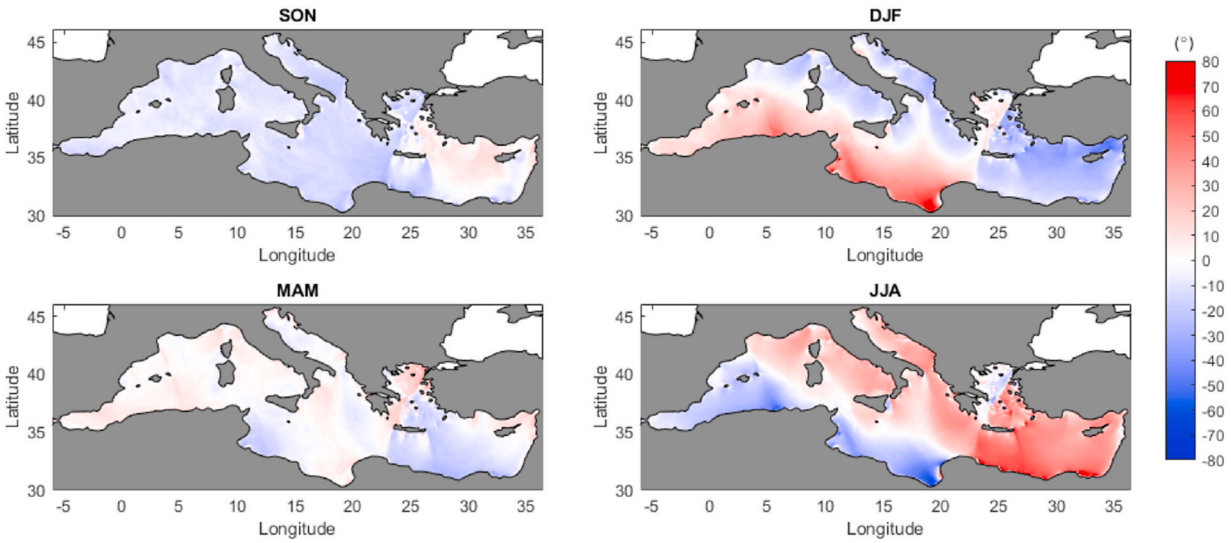

Fig. 12. Seasonal anomaly of the mean hourly wave direction, $\Delta\theta_{ms}$, during the 1961–2018 period. Each subpanel corresponds with a season, SON is autumn; DJF is winter, MAM is spring; and JJA is summer. The blue and red colors refer to a seasonal clockwise (CW) and counter-clockwise (CCW) turning of the θ_{ms}, respectively.

CMS. The large intra-annual variabilities identified in this study indicate that the annual mean hourly wave direction can be a very inaccurate indicator of wave directionality in the MS.

5.4. Wave climate interannual variability in the MS

This subsection explores the interannual variability in the MS wave climate by assessing the correlations of the monthly $H_{s,50}$ and $H_{s,99.5}$ ($H_{s,50monthly}$ and $H_{s,99.5monthly}$) values with climatic indices. Here, $H_{s,50monthly}$ and $H_{s,99.5monthly}$ were computed as the 50th and 99.5th percentiles, respectively, of the PDF of every month during each year throughout the 1961–2018 period. Similarly, the monthly mean surface wind speed ($U_{10,50monthly}$) was estimated. The five most meaningful climatic indices in the MS basin, the North Atlantic Oscillation (NAO), the East Atlantic-West Russia (EAWR) index, the East Atlantic index (EA), the Mediterranean Oscillation Index (MOI), and the Scandinavian (SCAND) pattern, were selected according to Criado-Aldeanueva and Soto-Navarro (2020) and Morales-Márquez et al. (2020).

The NAO represents a dipolar sea level pressure (SLP) characteristic pattern over the North Atlantic-European region with one centre in Iceland and the other in the Azores. The EA pattern is described as the SLP anomaly between the British Islands-Baltic Sea area and Greenland (Criado-Aldeanueva and Soto-Navarro, 2020). The MOI is defined as the dipolar behaviour of the atmosphere between the western and eastern MS, i.e., the normalized SLP difference between Marseille and Jerusalem. The EAWR pattern consists of four main anomaly centres. The positive phase is associated with positive height anomalies located over Europe and northern China and negative height anomalies located over the central North Atlantic and the northern Caspian Sea. Finally, the SCAND pattern consists of a primary circulation centre over Scandinavia, with relatively weak centres of opposite signs over western Europe and eastern Russia/western Mongolia. More detailed information about these climatic indices can be obtained from the Climate Prediction Center (CPC) and the Physical Sciences Laboratory (PSL) of the National Oceanic and Atmospheric Administration (NOAA) at the following webpages: https://www.cpc.ncep.noaa.gov/data/teledoc/telecontents.shtml and https://psl.noaa.gov/gcos_wgsp/Timeseries/.

Table 3 presents the correlation coefficients between both $H_{s,50monthly}$ and $U_{10,50monthly}$ and the climatic indices, providing spatially averaged values over the entire MS basin, the EMS, the CMS, and the WMS. Figs. 13 and 14 display correlation maps of $H_{s,50monthly}$ and $H_{s,99.5monthly}$, respectively, for the months of January, April, and August.

The correlations between $H_{s,50monthly}$ and the NAO were found to be statistically significant (at the 90% confidence interval) and positive in the northern EMS (Aegean Sea) during the summer months, with values reaching 0.40. In contrast, negative correlations were found in the WMS and northern CMS, both during the summer months. Nonetheless, in the WMS, relatively high significant correlations with values down to −0.5 were found during the autumn, winter, and spring seasons (see Table 3). Moreover, these correlations were significant and negative in the Adriatic Sea in the winter. For $U_{10,50monthly}$, the NAO displayed correlations of −0.27 during winter in the WMS and values reaching 0.35 and 0.42 during summer and autumn, respectively, in the EMS. The results most often showed similar behaviours involving high correlations between NAO and both $H_{s,50monthly}$ and $U_{10,50monthly}$ in the same area during the same season.

The MOI correlations with $H_{s,50monthly}$ were statistically significant and positive over almost the whole MS basin during the winter months, with large values reaching 0.6 and 0.56 in the CMS and WMS, respectively. These high values could be attributed to the strong correlations between MOI and $U_{10,50monthly}$ during winter, with values up to 0.85 and 0.72 in the WMS and CMS, respectively (see Table 3). Notably, in the WMS and CMS, the correlations with $H_{s,50monthly}$ were positive for almost the entire year. The Tyrrhenian Sea was characterized by significant $H_{s,50monthly}$ correlations, with values reaching 0.5 in every season.

For the EA index, the correlations with $H_{s,50monthly}$ were negative in a large extent of the MS basin and were relatively large in the EMS, with correlation values down to −0.64 in August and −0.48 for $U_{10,50monthly}$. Additionally, the correlations were also negative in the CMS and WMS, with values down to −0.6 in May for the CMS and down to −0.42 in December for the WMS (see Table 3). Statistically significant values were found in the Levantine Sea throughout the entire year, in the Tyrrhenian Sea and CMS in August, and in the Gulf of Lyon and the Adriatic Sea in January.

The correlations between the EAWR index and $H_{s,50monthly}$ were positive and significant in the EMS, with values reaching 0.34 in August. However, the correlations were negative and significant, with values down to −0.36 and −0.54 in the CMS and WMS, respectively, during winter (December and January) (see Fig. 13 and Table 3). During this season, EAWR showed correlation values of −0.35 and −0.25 with $U_{10,50monthly}$ in the WMS and CMS, respectively.

Finally, the SCAND pattern exhibited positive correlations with $H_{s,50monthly}$ in most of the MS basin in the summer (August), with values reaching 0.42 in the EMS and a correlation of 0.43 with $U_{10,50monthly}$.

Table 3
Correlation coefficients between the $H_{s,50monthly}$ and five climatic indices in the whole Mediterranean Sea as well as sub-regions during the 1961–2018 period. Values in parenthesis are the correlation coefficients between $U_{10,50monthly}$ and the five climatic indices. $U_{10,50monthly}$ is shown when the absolute values are larger than 0.25 and when that of $H_{s,50monthly}$ is also larger than 0.25.

period	Full Mediterranean Sea (FMS)					Eastern Mediterranean Sea (EMS)					Central Mediterranean Sea (CMS)					Western Mediterranean Sea (WMS)				
	NAO	EAWR	MOI	EA	SCAND	NAO	EAWR	MOI	EA	SCAND	NAO	EAWR	MOI	EA	SCAND	NAO	EAWR	MOI	EA	SCAND
January	–	−0.36	0.60 (0.69)	–	–	–	–	0.49 (0.25)	−0.342 (−0.33)	–	–	−0.36	0.60 (0.72)	–	–	−0.273	−0.39 (−0.30)	0.54 (0.80)	–	–
February	−0.47	–	–	−0.37	0.25	−0.27	–	–	−0.41	–	−0.40	–	–	−0.39	0.26	−0.43 (−0.27)	−0.44 (−0.51)	0.33 (0.64)	−0.26	–
March	−0.315	–	0.27 (0.48)	0.288	0.264	–	–	–	–	–	–	–	–	–	0.34 (−0.26)	−0.37	–	0.28 (0.62)	−0.27	–
April	–	–	0.37 (0.35)	–	–	–	–	–	−0.41	–	–	–	0.28	−0.262	–	–	−0.27	0.56 (0.61)	–	0.34
May	0.281	−0.274	0.28	−0.46	–	–	–	–	−0.25 (0.27)	–	–	−0.257	–	−0.60	–	−0.26	−0.35	0.27 (0.29)	−0.27	–
June	0.35	–	0.42	–	–	0.37 (0.35)	–	–	–	–	–	–	0.31	–	0.258 (−0.30)	–	–	0.365	–	–
July	0.47	−0.264	0.29	–	–	0.40 (0.27)	–	–	–	–	–	–	0.33	–	–	–	−0.36	0.28	–	–
August	−0.25 (0.31)	–	–	−0.43	0.41	–	0.34	–	−0.64 (−0.48)	0.42 (0.43)	–	–	–	−0.29 (0.36)	0.376	−0.34	–	–	–	0.27
September	−0.26 (0.47)	–	0.30	–	–	–	–	–	–	–	–	–	0.25	–	–	−0.51	–	0.36	–	0.37 (−0.29)
October	–	–	–	−0.29	–	0.25 (0.42)	–	–	–	–	–	–	–	–	–	−0.40	–	0.29 (0.28)	−0.36	–
November	–	–	–	−0.343	–	0.28 (0.35)	–	–	–	–	–	–	–	−0.254	–	−0.44	−0.26 (−0.31)	–	−0.28	–
December	−0.25	−0.39	0.48 (0.63)	−0.39	–	–	–	–	–	–	–	−0.35 (−0.25)	0.44 (0.66)	−0.41	–	–	−0.54 (−0.35)	0.56 (0.85)	−0.42	–

- indicates absolute values of the correlation coefficients, for $H_{s,50monthly}$, lower than 0.25.

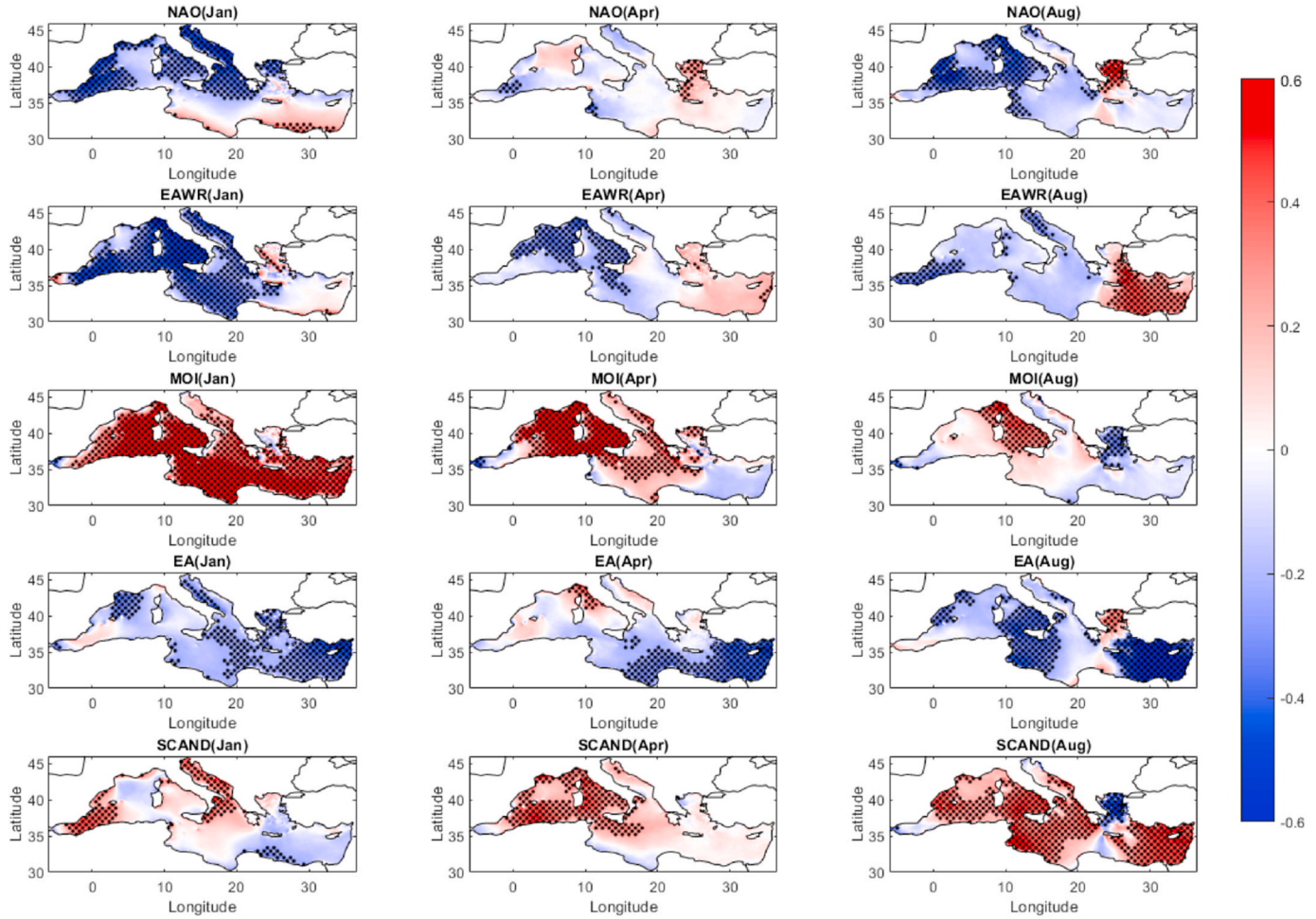

Fig. 13. Spatial correlation coefficients between $H_{s,50monthly}$ and five climatic indices (NAO, EAWR, MOI, EA, and SCAND) during January, April and August (1961–2018). Areas with statistically significant correlations at the 90% confidence interval (tested with Mann-Kendall test) are stippled by black dots.

These correlations were also positive and significant in the CMS during February and March (see Table 3) and in the Adriatic Sea in January, where the values reached 0.4 (see Fig. 13). Moreover, significant positive correlations occurred in the WMS during the autumn (September) and spring (April) (see Table 3).

Regarding the spatial correlations between $H_{s,99.5monthly}$ and the five selected climate indices (NAO, EAWR, EA, MOI, and SCAND), despite the quite similar correlation patterns observed for both the mean and extreme conditions, the spatial distribution of statistically significant correlations were different than those of $H_{s,50monthly}$ (see Figs. 13 and 14). For example, EAWR displayed significant values for $H_{s,50monthly}$ at the Sardinian Sea in April but less significance for $H_{s,99.5monthly}$.

At the seasonal level, the spatial patterns in the correlations between $H_{s,50monthly}$ or $H_{s,99.5monthly}$ and the 5 climate indices were almost similar during summer and winter for each index. However, they exhibited different spatial distributions of statistically significant correlations. The MOI revealed the largest positive significant values in the MS basin during winter. Additionally, the SCAND index exhibited a positive significant correlation during summer. In contrast, the EA index displayed significant negative correlations in the EMS (Levantine Sea) during summer for both $H_{s,50monthly}$ and $H_{s,99.5monthly}$ (see Figs. 13 and 14).

5.5. Wave storminess in the MS basin

This subsection analyses the frequency of extreme events in the MS basin by analysing the number of storms occurring per year. Mentaschi et al. (2015) defined a typical storm in the MS basin as an event with $H_s > 4$ m; this definition agrees with the spatially averaged $H_{s,99.5}$ value found in this study (4.2 m). Consequently, in the current study, we used this value as a threshold to first identify the number of independent events with $H_s > 4.2$ m; next, we quantified the number of storms per year (N); and finally, we defined the average number of storms per year (N_{op}). To guarantee independence, successive storms that took place within a period shorter than 72 h were considered a single event. Fig. 15 shows the spatial distribution of N_{op} in the MS basin for the 58-year period. The western WMS was the most stormy area in the MS basin during this time, with a typical N_{op} exceeding 3 storms/year as shown in the Sardinian Sea, where the strong Mistral winds dominate. The Tyrrhenian Sea in the WMS and the Ionian Sea in the CMS showed N_{op} values reaching 2 storms/year. The Adriatic Sea in the CMS and the Aegean and Levantine Seas in the EMS exhibited fewer storms per year ($N_{op} < 2$ storms/year). Exceptions were found in the jet-like-pattern area located southern to Crete and generated by the Etesian winds that dominate in the Aegean Sea, in addition to the southern Adriatic Sea dominated by the Sirocco winds, with N_{op} values of ~2 storms/year.

5.6. Long-term trends in the wave climatology of the MS

In this subsection, the $H_{s,50}$ and $H_{s,99.5}$ trends (trend $H_{s,50}$ and trend $H_{s,99.5}$), as representatives of the mean and extreme regimes in the MS basin, are presented. These trends were obtained by fitting a linear regression model to the hourly data in the 1961–2018 period. The model consisted of a slope coefficient and an independent term. Maps displaying the spatial distribution of these trends (i.e., the slope coefficient

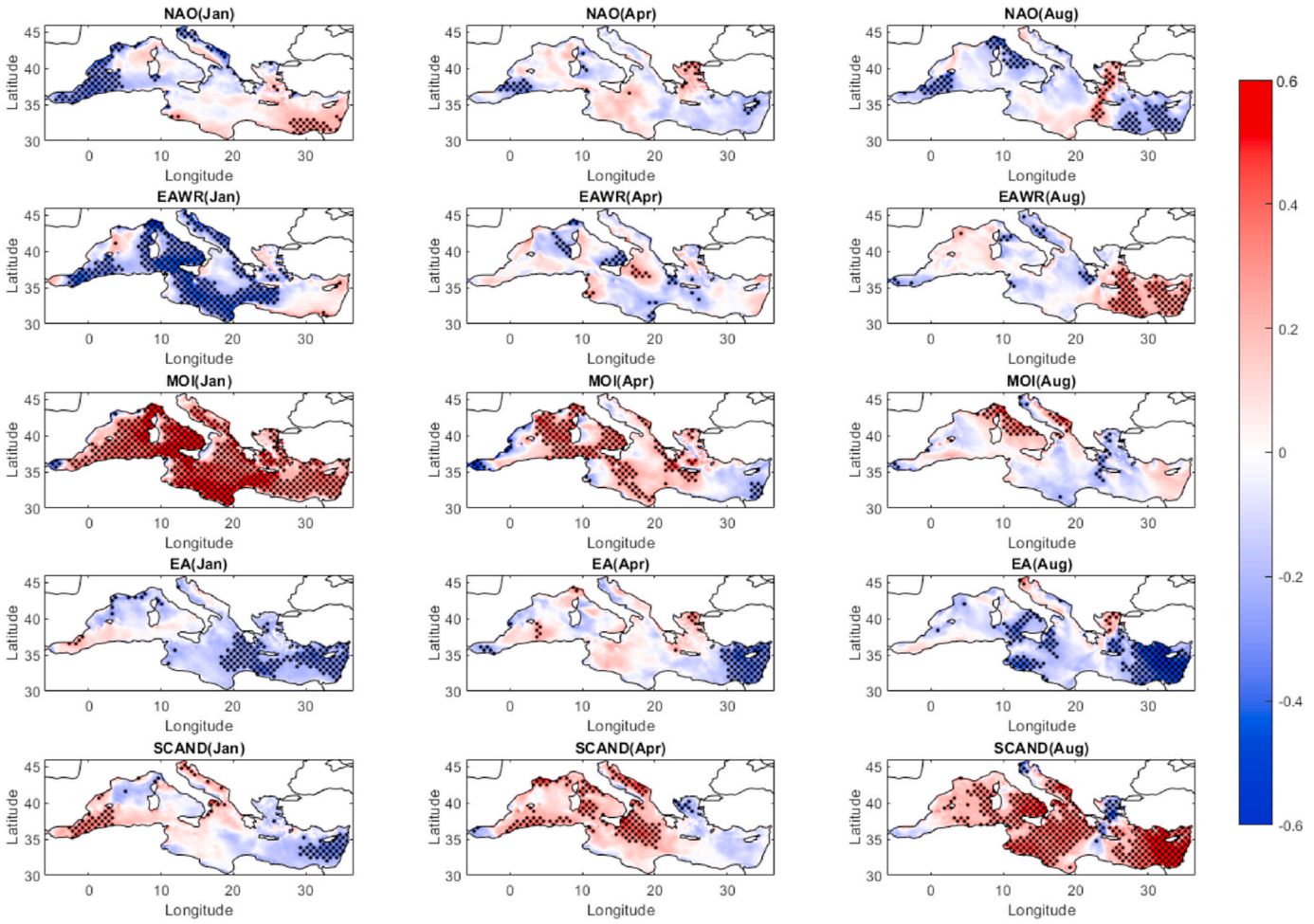

Fig. 14. Spatial correlation coefficients between $H_{s,99.5monthly}$ and five climatic indices (NAO, EAWR, MOI, EA, and SCAND) during January, April and August (1961–2018). Areas with statistically significant correlations at the 90% confidence interval (tested with Mann-Kendall test) are stippled by black dots.

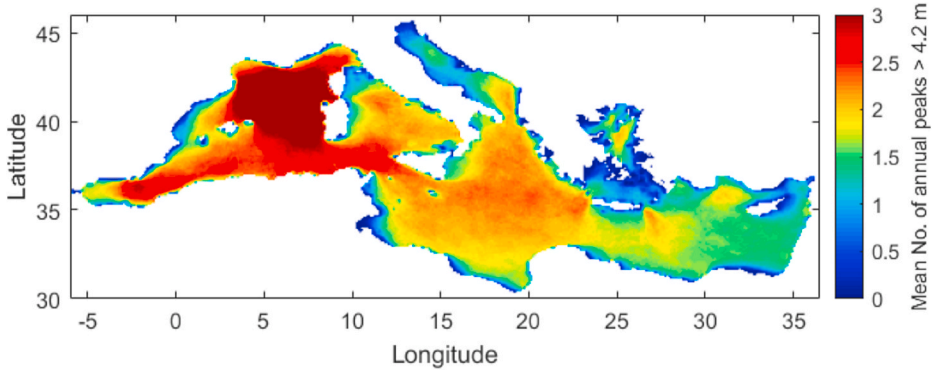

Fig. 15. Average number of storms per year (N_{op}) with $H_s > 4.2$ m in the MS basin during the 1961–2018 period.

of the regression model) are shown in Figs. 16 and 17 for the whole period (trends in the interannual variability) and the different seasons (trends in the intra-annual variability), respectively. The trends are mapped in cm/decade, and stippling points are shown where the trends were found to be statistically significant at the 90% confidence level using the Mann-Kendall test (Mann, 1945; Kendall, 1975). The spatially averaged values of the seasonal trends are listed in Table 4 for the full MS (FMS) basin and sub-regions. The trends were also computed for the entire 58-year period.

The spatial average of the $H_{s,50}$ trend in the MS basin (shown in panel A of Fig. 16) was negative and statistically significant, with a magnitude of −0.4 cm/decade. The $H_{s,50}$ trend was negative in most of the MS basin, except in the Alboran, Adriatic, and Sardinian Seas, where the trends were positive. For example, in the Levantine Sea, the trends are negative and statistically significant in the area between Egypt and Turkey, with values down to −2 cm/decade, whereas in the Alboran Sea, the trends were positive and statistically significant, with magnitudes reaching 2 cm/decade.

Additionally, the spatial average of the $H_{s,99.5}$ trend in the MS basin, as a consequence of the spatially distributed negative and positive

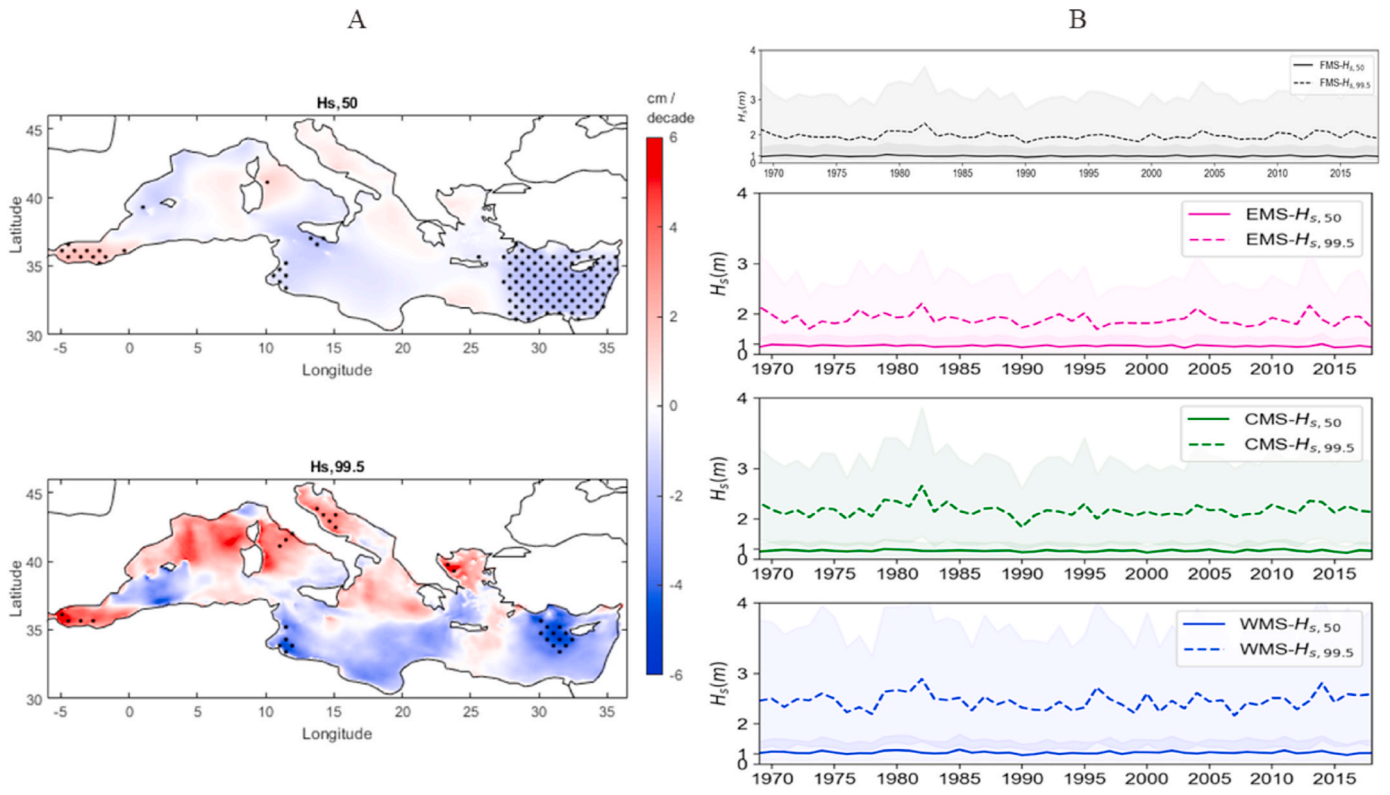

Fig. 16. Panel A shows the $H_{s,50}$ trend (upper) and $H_{s,99.5}$ trend (lower) in the MS basin during the 1961–2018 period. Areas with statistically significant trends with a 90% confidence level (tested with Mann-Kendall test) are stippled by black dots. The trends are plotted in cm/decade. Panel B shows the spatial mean (coloured lines) and standard deviation (filled area) of the annual $H_{s,50}$ and $H_{s,99.5}$ calculated for the full, eastern, central, and western MS basins (FMS, EMS, CMS, WMS, respectively).

patterns (panel A of Fig. 16), was negligible (0.11 cm/decade). These patterns were positive in the northern (north Sardinian, north Adriatic, and north Aegean Seas) and south-western (the Alboran Sea) MS basin and negative in the southern CMS and in the Levantine Sea. Notably, the $H_{s,99.5}$ trend was statistically significant and positive, with values reaching 4 cm/decade, in sub-regions of these sub-basins, for example, in the Alboran Sea and the northern parts of the Adriatic and Tyrrhenian Seas. In contrast, the $H_{s,99.5}$ trend was statistically significant and negative in the Levantine Sea, with values reaching −4 cm/decade.

Panel B of Fig. 16 shows the time series of the spatial mean and the standard deviation of the annual $H_{s,50}$ and $H_{s,99.5}$ values calculated for the FMS, EMS, CMS, and WMS basins. The results indicate that mild changes took place throughout the 58-year period in both the annual $H_{s,50}$ and annual $H_{s,99.5}$, with larger standard deviations and variabilities observed in $H_{s,99.5}$ than in $H_{s,50}$ in all basins.

The spatial pattern of the seasonal $H_{s,50}$ trend was negative in most areas of the MS basin during the winter, spring, and summer seasons and positive in autumn in the sub-basins of the CMS and WMS (Fig. 17). An exception was found in the Alboran Sea of the WMS, where the $H_{s,50}$ trend was positive during all seasons. The seasonal $H_{s,50}$ trends were statistically significant in the Levantine Sea and the CMS areas during summer, with values of −3 cm/decade, and in the WMS during autumn, with moderate values of 1.2 cm/decade.

The spatial pattern of the seasonal $H_{s,99.5}$ trend was consistently steeper than that of the $H_{s,50}$ trend, and more importantly, the spatial patterns are different, especially during the winter and spring seasons (Fig. 17, Table 4). In winter, a positive $H_{s,99.5}$ trend was found in the southern Levantine Sea in the EMS (with rates up to 6 cm/decade) and negative $H_{s,99.5}$ trends were found in the Tyrrhenian Sea and in the southern Sardinian Sea along the Algerian coasts in the WMS (rates down to −6 cm/decade). In summer, positive, statistically significant $H_{s,99.5}$ trends (up to 6 cm/decade) were found in the Alboran, northern Sardinian and Tyrrhenian Seas in the WMS and in the Adriatic Sea in the CMS. In contrast, negative, statistically significant $H_{s,99.5}$ trends (down to −6 cm/decade) were found in the Levantine Sea (EMS), the Ionian Sea (CMS), and along the eastern Spanish coast (WMS) during the same season. For a more detailed interpretation of the spatial seasonal $H_{s,99.5}$ trends, refer to Fig. 17.

In summary, during the 1961–2018 period, decreasing trends in $H_{s,50}$ and $H_{s,99.5}$ were consistently found in the MS wave climate throughout the winter, spring, and summer seasons and increased during autumn, with larger $H_{s,99.5}$ rates than $H_{s,50}$ rates.

Regarding the long-term storminess trends in the MS, the trends in N were also analysed throughout the 1961–2018 period using the same model as described above. Identifying trends in N is key when performing extreme value analyses, as an increase in the frequency of storms would consequently increase the estimated return-period values. As shown in Fig. A.8, the trends in N were very mild in the MS basin throughout the study period. The results revealed mild statistically significant negative trends in the Gulf of Lyon in the northern Sardinian Sea in the WMS and in the south-western Levantine Sea in the EMS, with a decrease rate of −2%. Additionally, slightly positive trends were found in the Alboran Sea, Balearic Sea and Aegean Sea.

6. Conclusions

The wind-wave climatology in the MS was presented and discussed in the current study based on a 58-year, high-resolution MS wave hindcast. The state-of-the-art spectral wind wave model WW3 was used to develop the MS wave model to produce a hindcast for the 1961–2018 period. The MS wave hindcast provides hourly time series of the sea state parameters; spectral partitioned wave data at a spatial resolution of 0.1° in both longitude and latitude; and a 3-h time series of the directional wave spectra along the coastal areas of the MS basin, with a

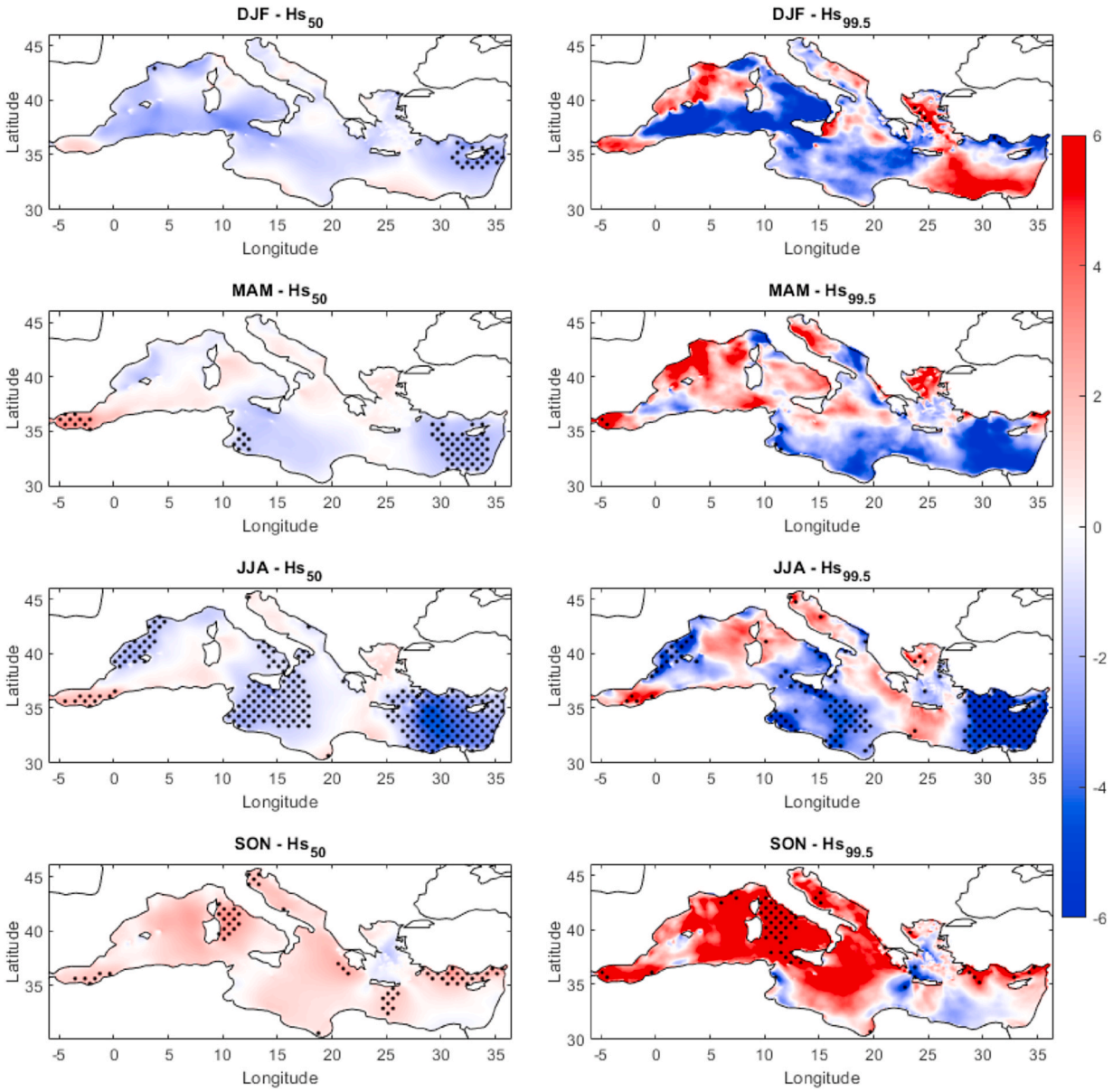

Fig. 17. Seasonal trends of $H_{s,50}$ and $H_{s,99.5}$ in the MS basin during the period 1961–2018. The row-wise allocated subpanels indicate the seasons (DJF: winter, MAM: spring, JJA: summer, SON: autumn). The column-wise subpanels refer to the $H_{s,50}$ and $H_{s,99.5}$. Areas with statistically significant trends at the 90% confidence interval (tested with Mann-Kendall test) are stippled by black dots. The trends are plotted in cm/decade.

Table 4
Spatial averages over the MS and sub-regions of $H_{s,50}$ and $H_{s,99.5}$ seasonal trends (cm/decade) during the 1961–2018 period.

Season	$H_{s,50}$				$H_{s,99.5}$			
	FMS	WMS	CMS	EMS	FMS	WMS	CMS	EMS
Winter (DJF)	−0.944	−1.233	−0.866	−1.136	0.46	−1.875	−2.337	1.346
Spring (MAM)	−0.40	0.12	−0.753	−1.376	−0.096	1.71	−1.385	−3.546
Summer (JJA)	−0.897	−0.235	−0.897	−2.95	−1.726	−0.087	−2.268	−5.33
Autumn (SON)	0.841	1.20	0.8965	0.5624	2.223	5.5487	3.17	1.036

spacing of 0.2°. The dataset obtained herein represents one of the longest wave datasets representing the MS to date.

The MS wave model was forced with the high-resolution UERRA-MESCAN-SURFEX wind fields (at a 5.5-km horizontal resolution). The source-term parameterization was set to T405, the recommended physical wind input and dissipation formulation developed by Ardhuin et al. (2010) for short-fetch regions. The wind wave growth parameter $\beta_{\max}$ was used for the model calibration, using satellite altimeter data collected during 2011 as a benchmark. The calibration procedure applied in the current study optimized the $\beta_{\max}$ parameter to minimize the residual error of H_s at the 10th, 50th, 99th, and 99.5th percentiles; in addition, a convergence criterion was set for this error at $\pm$ 0.1 m. In the MS, the optimal $\beta_{\max}$ value was found to be 2.25 for the employed forcing wind fields.

The validation of the dataset was carried out against records collected by 26 wave buoys in the MS basin and more than 27 years of recalibrated and denoised altimeter H_s data. The validation results displayed strong agreement between the H_s values provided by the MS wave hindcast and the in situ observations recorded at buoys, with negligible positive biases and linear regression slopes close to 1 for the wave parameter, H_s and T_m values. Furthermore, the dataset revealed a robust representation of θ_m in the MS basin with a bias less than 1°, likely because of the quality of the high-resolution wind fields. Comparing the wave dataset with the altimeter observations of H_s, the MS hindcast reported bias, RMSE, SI and correlation coefficient values of 0.022 m, 0.30 m, 0.2 and 0.93, respectively. Additionally, the distributions of H_s in the modelled dataset and altimeter observations for the MS basin as well as for the different MS sub-basins showed strong matches between both distributions when $H_s > 1$ m, with Pearson correlations exceeding 0.91. Accordingly, the validation of the MS wave hindcast, developed using the UERRA-MESCAN-SURFEX wind fields, showed that the data are appropriate for wave climate analyses.

The results show that there is a high presence of wind sea energy in the hourly wave spectra in the MS basin, although there is a slight influence of swell energy ($0.25 < WSF < 0.45$) in most of the MS basin. At the Gulf of Lyon (northern Sardinian Sea) and the Alboran Sea in the WMS, the Adriatic Sea in the CMS, and the Aegean Sea in the EMS, the wind sea is predominant ($WSF > 0.65$), corresponding with the wave generation domains attributed to the wind systems active in the MS basin.

The statistical characterization of the MS wave hindcast climate during the 1961–2018 period revealed that the spatially averaged H_s value varies between 1.1 m ($H_{s,50}$) and 4.20 m ($H_{s,99.5}$), while T_m ranges from 4.72 s ($T_{m,50}$) to 8 s ($T_{m,99.5}$). Additionally, the most energetic $H_{s,50}$ occurs in the WMS during winter and in the EMS during summer. However, the highest extreme waves occur in the WMS, mainly in the Sardinian Sea, throughout the whole year. Accordingly, the spatial distribution of the largest waves in the basin during mean conditions differed from that during extreme events. The directional wave climate in the MS basin revealed clear seasonal variability. The anomaly of the seasonal mean wave direction (θ_{ms}) relative to θ_m exhibits large values (reaching 60°), with opposing behaviours observed in the MS basin between the winter and summer seasons.

The correlations of the $H_{s,50monthly}$ and $H_{s,99.5monthly}$ values in the MS basin with five climate indices (NAO, EAWR, EA, MOI, and SCAND) revealed large, positive, and significant correlations with the MOI index during the winter. These correlations could be attributed to the high correlations, reaching 0.85, encountered in the MS between MOI and $U_{10,50monthly}$ during this season. During the summer season, the SCAND pattern exhibits statistically significant positive correlations in the MS basin with both $H_{s,50monthly}$ and $H_{s,99.5monthly}$. The results most often show similar behaviours of high correlations between the climatic indices and both $H_{s,50monthly}$ and $U_{10,50monthly}$ in the same area during the same season. For $H_{s,50monthly}$ and $H_{s,99.5monthly}$, the spatial correlation pattern is similar for each climate index; however, the significance of these correlations are differently distributed.

The WMS is the area characterized by the most frequent occurrence of storms (defined by the threshold $H_s > 4.2$ m), with $N_{op} > 3$ per year, whereas the EMS and the short-fetch sub-basins are characterized by less frequent stormy conditions, with $N_{op} < 2$ per year.

The MS wave climate in the 1961–2018 period shows negative trends in both $H_{s,50}$ and $H_{s,99.5}$ during winter, spring, and summer; in contrast, these trends are positive during autumn under both mean and extreme conditions, with the largest changes observed during extreme conditions. The spatial patterns of these trends differ mainly during mean and extreme conditions in the winter and spring seasons. In general, the long-term trends in $H_{s,50}$ and $H_{s,99.5}$ as well as the changes in N in the MS basin are found to be mild, with values reaching 6 cm/decade and less than 2% in the absolute value, respectively. Additionally, the EMS is characterized by statistically significant negative $H_{s,50}$ and $H_{s,99.5}$ trends, while the most western area of the WMS is characterized by statistically significant positive trends under both mean and extreme conditions.

Authorship contributions

Conception and design of study: Ahmed I. Elshinnawy and Jose A. Á. Antolínez. Acquisition of data and model setup, calibration, validation and wave dataset production: Ahmed I. Elshinnawy. Analysis and/or interpretation of data: Ahmed I. Elshinnawy and Jose A. Á. Antolínez.

Drafting the manuscript and revising the manuscript critically for important intellectual content: Ahmed I. Elshinnawy and Jose A. Á. Antolínez.

Approval of the version of the manuscript to be published: Ahmed I. Elshinnawy and Jose A. Á. Antolínez.

Declaration of competing interest

The authors declare that they have no known competing financial interests or personal relationships that could have appeared to influence the work reported in this paper.

Data availability

The UERRA-MESCAN-SURFEX wind fields is provided on the website of the Copernicus Climate Data Store (CDS): https://cds.climate.copernicus.eu/cdsapp#!/dataset/reanalysis-uerra-europe-single-levels?tab=overview. The ESA-CCI altimeter dataset is provided on the following website https://data.ceda.ac.uk/neodc/esacci/sea_state/data/v1.1_release/l2p/. The monthly time series of climate indices are available on the following website: https://www.cpc.ncep.noaa.gov/data/teledoc/telecontents.shtml. The buoy data is provided on the following website: https://resources.marine.copernicus.eu/product-detail/INSITU_MED_NRT_OBSERVATIONS_013_035/INFORMATION.

Acknowledgements

The work of the researcher Ahmed I. Elshinnawy is fully funded by a postdoc scholarship from the Ministry of Higher Education of the Arab Republic of Egypt. The authors would also like to thank the reviewers for their valuable suggestions and comments.

Appendix A. Figures and tables for the MS wave model calibration and validation

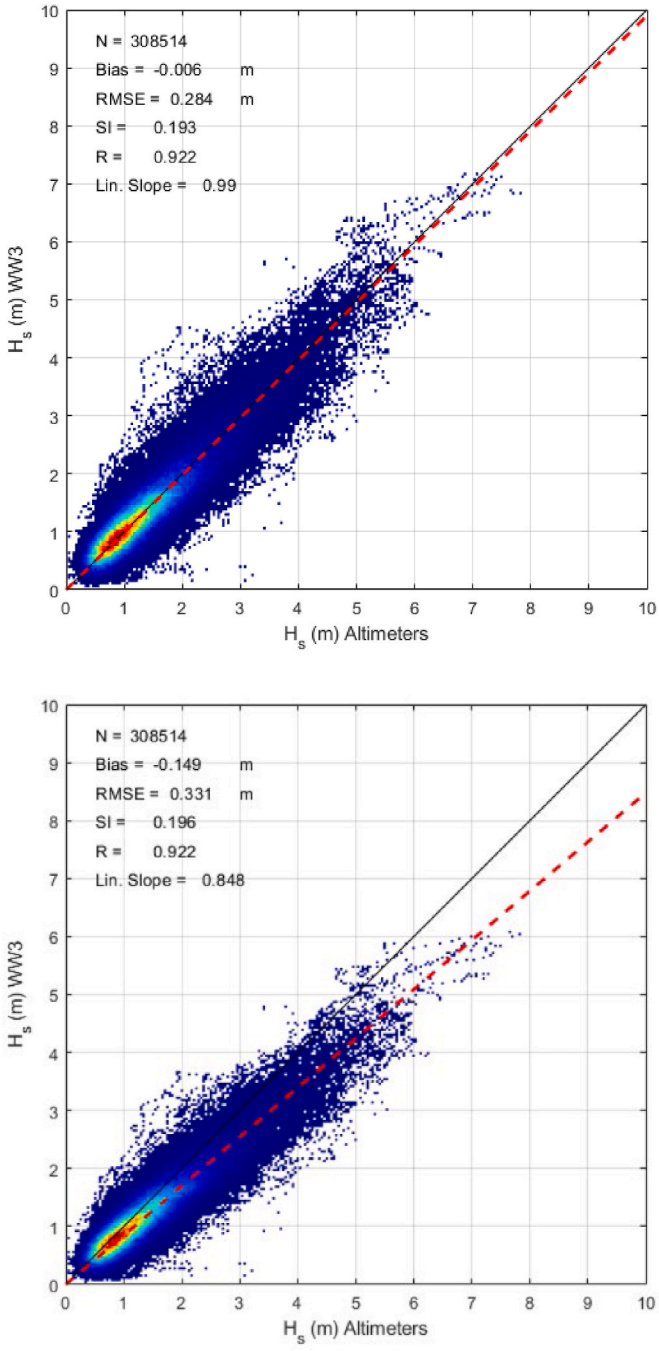

Fig. A.1. Scatter plots of H_s in the year 2011, the y-axis refers to the WW3 output (co-located along the satellite tracks), and the x-axis to the altimeter data, using the source term parameterization T405 with the optimum value of $\beta_{\max} = 2.25$ (upper panel) and the default value of $\beta_{\max} = 1.55$ (lower panel). The different error metrics are shown. The red dashed line, shown in each panel, represents the slope of the linear regression. The color intensity corresponds to the density of data.

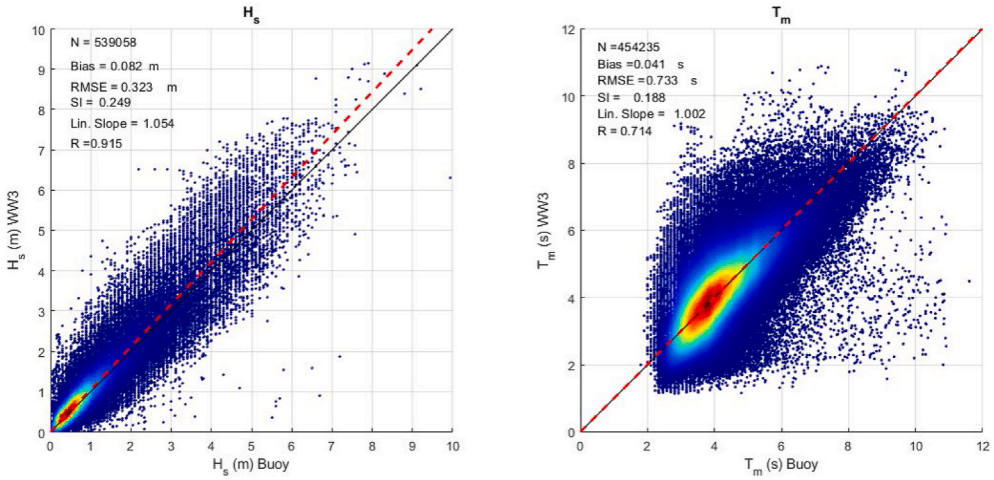

Fig. A.2. Scatter plots of the measured and modelled significant wave height (H_s) and the mean period (T_m) from in-situ wave buoys employed in the current study, using the source term parameterization T405 with the optimum value of $\beta_{\max} = 2.25$. The different error metrics (Bias, RMSE, SI, Pearson correlation R and the linear slope) are shown in both panels. The red dashed line, shown in each panel, represents the slope of the linear regression. The colour intensity corresponds to the density of data.

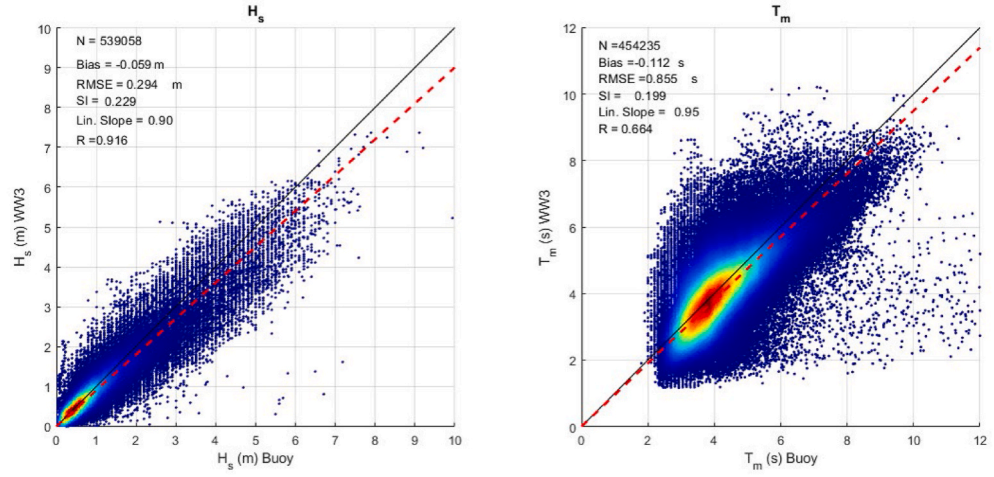

Fig. A.3. The same as Fig. A.2 but using the default value of $\beta_{\max} = 1.55$.

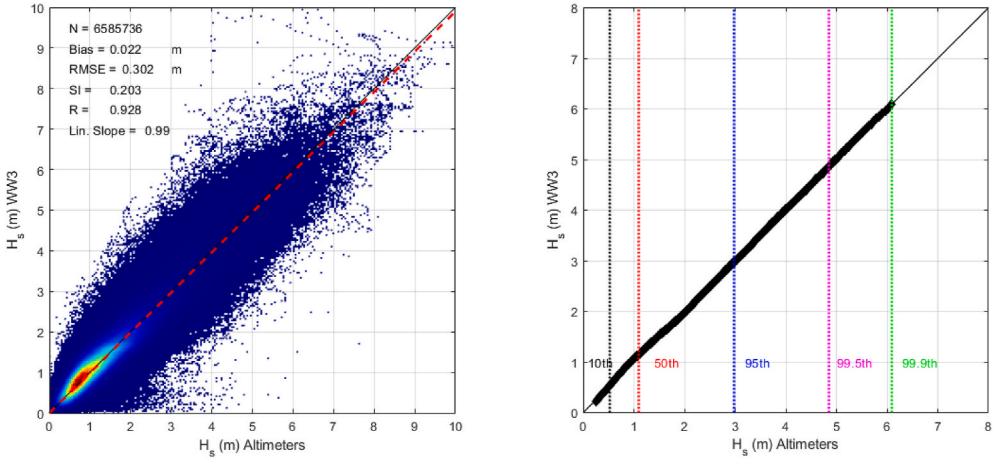

Fig. A.4. Left: A scatter plot of H_s pairs from the MS hindcast and the SSCCI altimeter database of H_s for the 1991–2018 period, showing different error metrics (Bias, RMSE, SI, Pearson correlation R and the linear slope). The red dashed line, shown in the left panel, represents the slope of the linear regression. The colour intensity corresponds to the density of data. Right: Quantile-Quantile plot for modelled and altimeter H_s for the whole period (1991–2018), with vertical lines corresponding to different percentiles of H_s. Results are shown using the source term parameterization T405 with the optimum value of $\beta_{\max} = 2.25$.

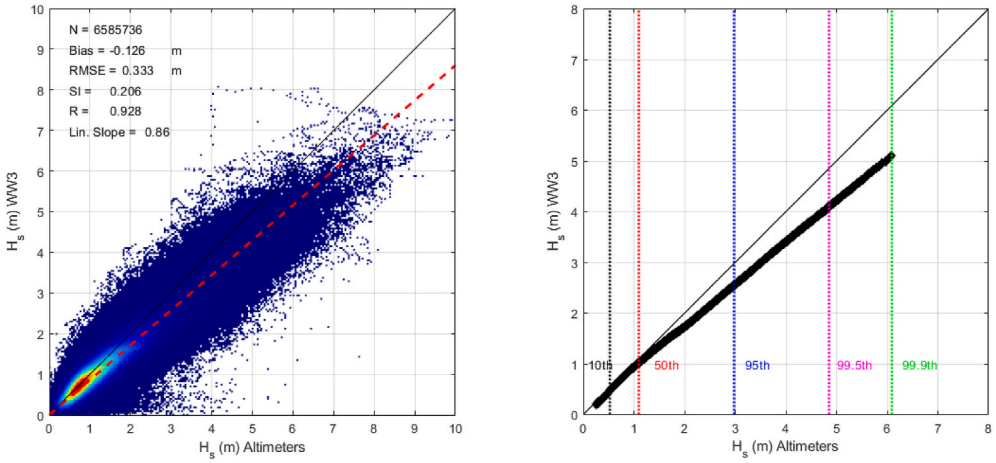

Fig. A.5. The same as Fig. A.4 but using the default value of $\beta_{\max} = 1.55$.

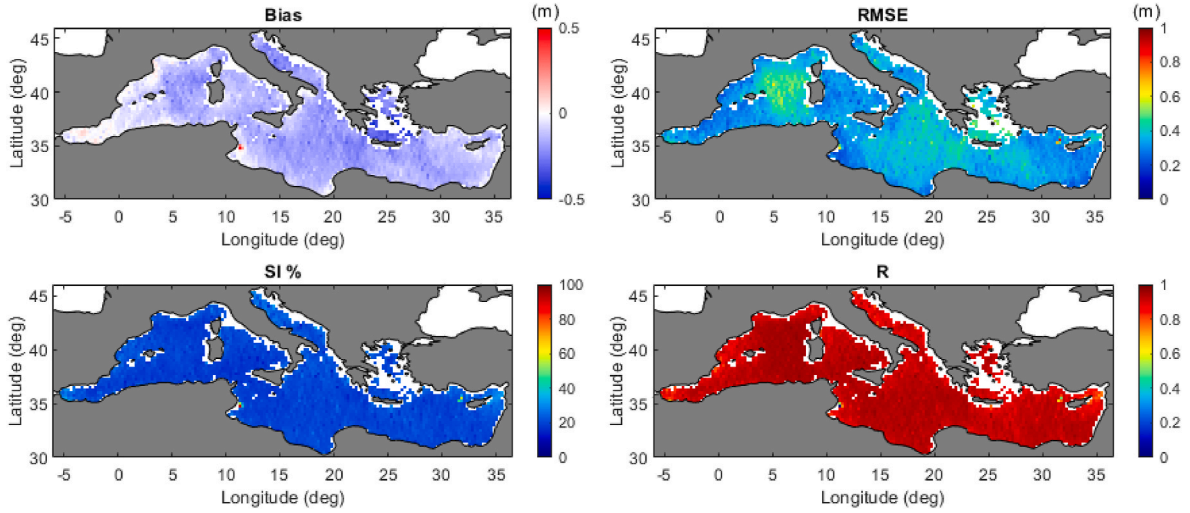

Fig. A.6. Spatial distributions of the Bias (Bias panel), the RMSE (RMSE panel), the scatter index (SI % panel), and the correlation coefficient (R panel) in H_s using the default value of $\beta_{\max} = 1.55$. The performance of the MS hindcast is evaluated using, as benchmark, the SSCCI altimeter data of H_s from 1991 to 2018.

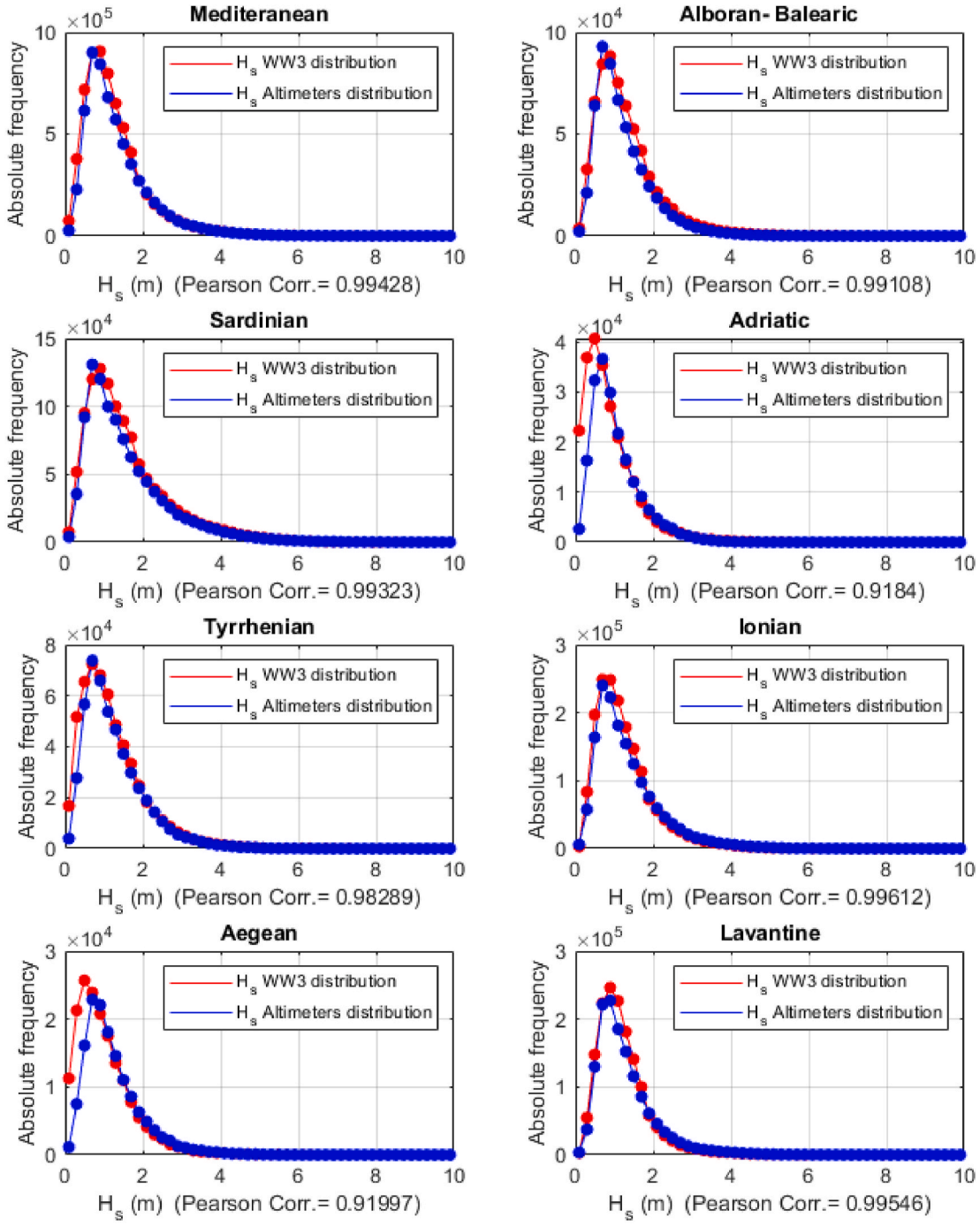

Fig. A.7. Histograms of H_s in the period 1991–2018. In blue the SSCCI altimeter data of H_s, and in red the corresponding output from WW3. Panel Mediterranean shows the histogram corresponding to the whole basin data and all the other for the several sub-basins. The model wave heights were spatially co-located along the satellite tracks. The Pearson correlation coefficient is provided in the x-axis label.

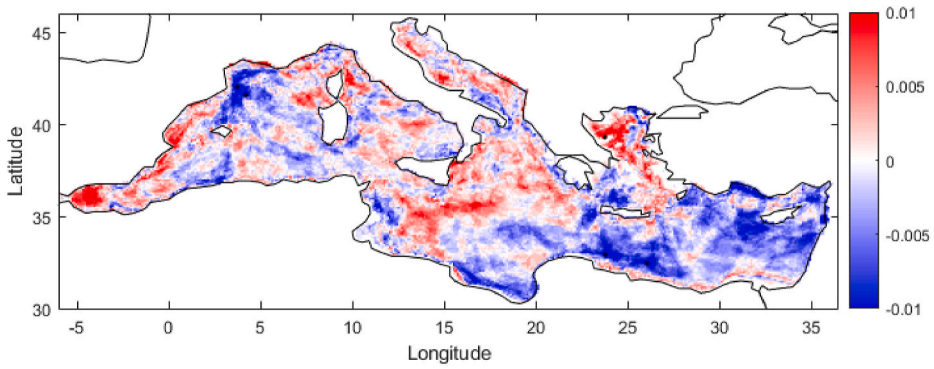

Fig. A.8. Trend of N, the number of storms per year, defined with a threshold $H_s > 4.2$ m in the MS basin during the 1961–2018 period. The trends are plotted in N/year. The color bar ranges between −1% and 1%, which is equivalent to a decrease/increase of N of 0.1 per year, i.e., a decrease/increase of N of 1 per decade. Red and blue colors refer to an increase and decrease in storminess, respectively. Areas with statistically significant trends at the 90% confidence interval (tested with Mann-Kendall test) are stippled by black dots.

Table A.1
Error metrics of the significant wave height, mean wave period and mean wave direction comparing the Mediterranean Sea hindcast results with observations from 26 in-situ wave buoys data.

Buoy				H_s					T_m					θ_m	
No.	Station name (ID)	Location		Bias (m)	RMSE (m)	SI	R	Lin. Slope	Bias (s)	RMSE (s)	SI	R	Lin. Slope	NBI_θ (%)	$NRMSE_\theta$
		longitude	latitude												
1	Mahon (61197)	4.42	39.72	0.093	0.326	0.197	0.92	1.016	0.182	0.651	0.136	0.80	1.032	0.716	0.102
2	Cabo de Palos (61417)	−0.33	37.65	0.086	0.276	0.22	0.90	1.047	0.304	0.762	0.172	0.665	1.067	−2.46	0.118
3	Cabo de Begur (61196)	3.64	41.92	0.27	0.50	0.25	0.93	1.17	0.107	0.56	0.13	0.823	1.023	−0.326	0.129
4	Cabo de Gata (61198)	−2.333	36.567	0.23	0.377	0.24	0.92	1.21	0.261	0.662	0.155	0.741	1.065	−1.218	0.1065
5	Drangonera (61430)	2.10	39.56	0.042	0.30	0.24	0.85	0.993	0.238	0.69	0.158	0.72	1.054	1.113	0.142
6	Tarragona (61280)	1.48	40.69	0.16	0.30	0.25	0.90	1.148	0.39	0.768	0.172	0.667	1.095	−0.654	0.121
7	Valencia (61281)	0.208	39.517	−0.02	0.26	0.27	0.85	0.91	0.397	0.92	0.22	0.652	1.1	−1.862	0.128
8	Lion (61002)	4.7	42.1	0.13	0.38	0.19	0.953	1.056	–	–	–	–	–	–	–
9	Cote de Azur (61001)	7.8	43.4	0.16	0.386	0.283	0.92	1.15	–	–	–	–	–	–	–
10	Athos (61X03)	24.7	40.00	−0.058	0.273	0.235	0.94	0.95	−0.66	0.834	0.13	0.83	0.831	1.836	0.135
11	Lesvo (61X04)	25.80	39.10	−0.082	0.241	0.238	0.916	0.923	−0.356	0.55	0.116	0.856	0.90	2.536	0.09
12	Mykonos (61X05)	25.5	37.50	−0.12	0.297	0.217	0.931	0.883	−0.373	0.61	0.1277	0.863	0.903	1.652	0.101
13	Pylos (61X08)	21.6	36.80	−0.08	0.256	0.207	0.867	0.873	0.021	0.694	0.163	0.682	0.993	−2.78	0.093
14	E1M3 A (61X07)	24.90	35.80	−0.09	0.248	0.23	0.73	0.85	0.477	0.717	0.126	0.633	0.834	−1.644	0.101
15	Santo (61X06)	25.50	36.30	−0.13	0.292	0.25	0.89	0.874	−0.347	0.697	0.158	0.704	0.903	−2.23	0.142
16	Mazara (61208)	12.53	37.52	0.08	0.234	0.23	0.923	1.05	−0.256	0.911	0.177	0.67	0.935	−1.036	0.1137
17	Palermo (61209)	13.33	38.26	−0.02	0.215	0.20	0.95	0.94	−0.605	1.417	0.24	0.51	0.845	−2.425	0.12
18	Crotone (61210)	17.22	39.02	0.047	0.238	0.26	0.92	0.998	0.15	0.975	0.206	0.617	1.02	6.98	0.146
19	Cetraro (61211)	15.92	39.45	0.10	0.252	0.23	0.936	1.082	−0.2	0.952	0.18	0.718	0.945	4.79	0.1123
20	Alghero (61213)	8.11	40.55	0.025	0.314	0.19	0.96	0.951	−0.01	0.846	0.151	0.818	0.982	−1.47	0.09
21	Ponza (61214)	12.95	40.87	0.011	0.25	0.237	0.93	0.98	−0.123	0.8727	0.187	0.683	0.961	2.75	0.126
22	Monopoli (61215)	17.38	40.97	0.045	0.251	0.31	0.90	1.07	−0.66	0.991	0.164	0.69	0.851	2.14	0.105
23	Civitavecchia (61216)	11.55	42.24	0.182	0.313	0.343	0.92	1.265	−0.171	0.917	0.197	0.625	0.954	1.817	0.103
24	La Spezia (61219)	9.83	43.93	0.044	0.228	0.232	0.94	1.034	−0.197	0.97	0.188	0.70	0.95	0.532	0.123
25	Punta Maestra (61220)	12.52	45.33	0.033	0.265	0.425	0.84	1.03	−0.795	1.19	0.213	0.53	0.80	0.573	0.123
26	Cagliari (61221)	9.40	39.12	0.148	0.273	0.29	0.883	1.16	0.433	1.106	0.21	0.686	1.083	2.136	0.089

References

Albuquerque, J., Antolínez, J.A.A., Gorman, R.M., Méndez, F.J., Coco, G., 2021. Seas and swells throughout New Zealand: a new partitioned hindcast. Ocean Model. 168, 101897 https://doi.org/10.1016/j.ocemod.2021.101897.

Alday, M., Accensi, M., Ardhuin, F., Dodet, G., 2021. A global wave parameter database for geophysical applications. Part 3: improved forcing and spectral resolution. Ocean Model. 166, 101848 https://doi.org/10.1016/j.ocemod.2021.101848.

Amante, C., Eakins, B.W., 2009. ETOPO1 1 arc-minute global relief model: procedures, data sources and analysis. NOAA Tech. Memo. NESDIS NGDC-24 19. https://doi.org/10.1594/PANGAEA.769615.

Amarouche, K., Akpinar, A., 2021. Increasing trend on stormwave intensity in the western mediterranean. Climate 9, 1–17. https://doi.org/10.3390/cli9010011.

Amarouche, K., Akpınar, A., Bachari, N.E.I., Çakmak, R.E., Houma, F., 2019. Evaluation of a high-resolution wave hindcast model SWAN for the West Mediterranean basin. Appl. Ocean Res. 84, 225–241. https://doi.org/10.1016/j.apor.2019.01.014.

Amarouche, K., Akpınar, A., Çakmak, R.E., Houma, F., Bachari, N.E.I., 2020. Assessment of storm events along the Algiers coast and their potential impacts. Ocean Eng 210, 107432. https://doi.org/10.1016/j.oceaneng.2020.107432.

Amarouche, K., Akpınar, A., Semedo, A., 2022a. Wave storm events in the Western Mediterranean Sea over four decades. Ocean Model. 170, 101933 https://doi.org/10.1016/j.ocemod.2021.101933.

Amarouche, K., Bingölbali, B., Akpinar, A., 2022b. New wind-wave climate records in the western Mediterranean Sea. Clim. Dynam. 58, 1899–1922. https://doi.org/10.1007/s00382-021-05997-1.

Antolínez, J.A.A., Murray, A.B., Méndez, F.J., Moore, L.J., Farley, G., Wood, J., 2018. Downscaling changing coastlines in a changing climate: the hybrid approach. J. Geophys. Res. Earth Surf. 123, 229–251. https://doi.org/10.1002/2017JF004367.

Ardhuin, F., Herbers, T.H.C., Jessen, P.F., O'Really, W.C., 2003. Swell transformation across the continental shelf. Part II: validation of a spectral energy balance equation. J. Phys. Oceanogr. 33, 1940–1953. https://doi.org/10.1175/1520-0485(2003)033<1940:STATCS>2.0.CO;2.

Ardhuin, F., Rogers, E., Babanin, A.V., Filipot, J.F., Magne, R., Roland, A., van der Westhuysen, A., Queffeulou, P., Lefevre, J.M., Aouf, L., Collard, F., 2010. Semiempirical dissipation source functions for ocean waves. Part I: definition, calibration, and validation. J. Phys. Oceanogr. 40, 1917–1941. https://doi.org/10.1175/2010JPO4324.1.

Ardhuin, F., Stopa, J.E., Chapron, B., Collard, F., Husson, R., Jensen, R.E., Johannessen, J., Mouche, A., Passaro, M., Quartly, G.D., Swail, V., Young, I., 2019. Observing sea states. Front. Mar. Sci. 6, 1–29. https://doi.org/10.3389/fmars.2019.00124.

Ayat, B., 2013. Wave power atlas of eastern mediterranean and aegean seas. Energy 54, 251–262. https://doi.org/10.1016/j.energy.2013.02.060.

Badriana, M.R., Lee, H.S., 2021. Multimodel ensemble projections of wave climate in the western north pacific using cmip6 marine surface winds. J. Mar. Sci. Eng. 9 https://doi.org/10.3390/jmse9080835.

Barbariol, F., Davison, S., Falcieri, F.M., Ferretti, R., Ricchi, A., Sclavo, M., Benetazzo, A., 2021. Wind waves in the Mediterranean Sea: an ERA5 reanalysis wind-based climatology. Front. Mar. Sci. 8, 1–23. https://doi.org/10.3389/fmars.2021.760614.

New York Battjes, J.A., Janssen, J.P.F.M., 1978. Energy loss and set-up due to breaking of random waves. In: Proceedings 16th International Conference Coastal Engineering, vol. 1. ASCE, Houston, TX, pp. 569–589, 10.9753/icce.v16.%25pp.

Bazile, E., Abida, R., Verelle, A., Le Moigne, P., Szczypta, C., 2017. MESCAN-SURFEX Surface Analysis, Deliverable D2.8 of the UERRA Project. http://www.uerra.eu/publications/deliverable-reports.html.

Bidlot, J., Janssen, P., Abdalla, S., 2007. A revised formulation of ocean wave dissipation and its model impact. In: Tech. Rep. Memorandum 509. ECMWF, Reading, U.K.

Boden, T.A., Marland, G., Andres, R.J., 2017. Global, Regional, and National Fossil-Fuel CO2 Emissions. Carbon Dioxide Information Analysis Center, Oak Ridge National Laboratory, U.S. Department of Energy, Oak Ridge, Tenn., U.S.A. https://doi.org/10.3334/CDIAC/00001_V2017.

Booij, N., Ris, R.C., Holthuijsen, L.H., 1999. A third-generation wave model for coastal regions. I- Model description and validation. J. Geophys. Res. 104, 7649–7666. https://doi.org/10.1029/98jc02622.

Caloiero, T., Aristodemo, F., Ferraro, D.A., 2022. Annual and seasonal trend detection of significant wave height, energy period and wave power in the Mediterranean Sea. Ocean Eng 243, 110322. https://doi.org/10.1016/j.oceaneng.2021.110322.

Camus, P., Mendez, F.J., Medina, R., Cofiño, A.S., 2011b. Analysis of clustering and selection algorithms for the study of multivariate wave climate. Coast. Eng. 58, 453–462. https://doi.org/10.1016/j.coastaleng.2011.02.003.

Cavaleri, L., Bertotti, L., 2004. Accuracy of the modelled wind and wave fields in enclosed seas. Tellus Dyn. Meteorol. Oceanogr. 56, 167–175. https://doi.org/10.3402/tellusa.v56i2.14398.

Cavaleri, L., Abdalla, S., Benetazzo, A., Bertotti, L., Bidlot, J.R., Breivik, Carniel, S., Jensen, R.E., Portilla-Yandun, J., Rogers, W.E., Roland, A., Sanchez-Arcilla, A., Smith, J.M., Staneva, J., Toledo, Y., van Vledder, G.P., van der Westhuysen, A.J., 2018. Wave modelling in coastal and inner seas. Prog. Oceanogr. 167, 164–233. https://doi.org/10.1016/j.pocean.2018.03.010.

Chawla, A., Tolman, H.L., 2008. Obstruction grids for spectral wave models. Ocean Model. 22, 12–25. https://doi.org/10.1016/j.ocemod.2008.01.003.

Chawla, A., Spindler, D.M., Tolman, H.L., 2013. Validation of a thirty year wave hindcast using the Climate Forecast System Reanalysis winds q. Ocean Model. 70, 189–206. https://doi.org/10.1016/j.ocemod.2012.07.005.

Criado-Aldeanueva, F., Soto-Navarro, J., 2020. Climatic indices over the mediterranean sea: a review. Appl. Sci. 10 https://doi.org/10.3390/app10175790.

De Leo, F., Besio, G., Mentaschi, L., 2021. Trends and variability of ocean waves under RCP8.5 emission scenario in the Mediterranean Sea. Ocean Dynam. 71, 97–117. https://doi.org/10.1007/s10236-020-01419-8.

de Schipper, M.A., Ludka, B.C., Raubenheimer, B., Luijendijk, A.P., Schlacher, T.A., 2021. Beach nourishment has complex implications for the future of sandy shores. Nat. Rev. Earth Environ. 2, 70–84. https://doi.org/10.1038/s43017-020-00109-9.

Dee, D.P., Uppala, S.M., Simmons, A.J., Berrisford, P., Poli, P., Kobayashi, S., Andrae, U., Balmaseda, M.A., Balsamo, G., Bauer, P., Bechtold, P., Beljaars, A.C.M., van de Berg, L., Bidlot, J., Bormann, N., Delsol, C., Dragani, R., Fuentes, M., Geer, A.J., Haimberger, L., Healy, S.B., Hersbach, H., Hólm, E.V., Isaksen, L., Kållberg, P., Köhler, M., Matricardi, M., Mcnally, A.P., Monge-Sanz, B.M., Morcrette, J.J., Park, B.K., Peubey, C., de Rosnay, P., Tavolato, C., Thépaut, J.N., Vitart, F., 2011. The ERA-Interim reanalysis: configuration and performance of the data assimilation system. Q. J. R. Meteorol. Soc. 137, 553–597. https://doi.org/10.1002/qj.828.

Dodet, G., Piolle, J.F., Quilfen, Y., Abdalla, S., Accensi, M., Ardhuin, F., Ash, E., Bidlot, J.R., Gommenginger, C., Marechal, G., Passaro, M., Quartly, G., Stopa, J., Timmermans, B., Young, I., Cipollini, P., Donlon, C., 2020. The Sea State CCI dataset v1: towards a sea state climate data record based on satellite observations. Earth Syst. Sci. Data 12, 1929–1951. https://doi.org/10.5194/essd-12-1929-2020.

Donatini, L., Lupieri, G., Contento, G., Pedroncini, A., Cusati, L.A., Crosta, A., 2015. MWM: a 35 years wind&wave high resolution hindcast dataset and an operational forecast service for the mediterranean sea. 18th Int. Conf. Ships Shipp. Res. NAV 2015, 116–125.

Elkut, A.E., Taha, M.T., Abu Zed, A.B.E., Eid, F.M., Abdallah, A.M., 2021. Wind-wave hindcast using modified ECMWF ERA-Interim wind field in the Mediterranean Sea. Estuar. Coast Shelf Sci. 252, 107267 https://doi.org/10.1016/j.ecss.2021.107267.

Elshinnawy, A.I., Medina, R., González, M., 2017. On the relation between the direction of the wave energy flux and the orientation of equilibrium beaches. Coast. Eng. 127, 20–36. https://doi.org/10.1016/j.coastaleng.2017.06.009.

Elshinnawy, A.I., Medina, R., González, M., 2018. Dynamic equilibrium planform of embayed beaches: Part 2. Design procedure and engineering applications. Coast. Eng. 135, 123–137. https://doi.org/10.1016/j.coastaleng.2018.01.001.

Elshinnawy, Ahmed I., Medina, R., Gonz, M., 2022a. In: Equilibrium Planform of Pocket Beaches behind Breakwater Gaps : on the Location of the Intersection Point, vol. 173. https://doi.org/10.1016/j.coastaleng.2022.104096.

Elshinnawy, Ahmed I., Medina, R., González, M., 2022b. Equilibrium planform of pocket beaches behind breakwater gaps: on the shape of the equilibrium shoreline. Coast. Eng. 174, 104112 https://doi.org/10.1016/j.coastaleng.2022.104112.

Erikson, L.H., Herdman, L., Flahnerty, C., Engelstad, A., Pusuluri, P., Barnard, P.L., Storlazzi, C.D., Beck, M., Reguero, B., Parker, K., 2022. Ocean Wave Time-Series Data Simulated with a Global-Scale Numerical Wave Model under the Influence of Projected CMIP6 Wind and Sea Ice Fields: U.S. Geological Survey Data Release. https://doi.org/10.5066/P9KR0RFM.

GlobWave, 2020. http://globwave.ifremer.fr/.

Gonçalves, M., Martinho, P., Guedes Soares, C., 2018. A 33-year hindcast on wave energy assessment in the western French coast. Energy 165, 790–801. https://doi.org/10.1016/j.energy.2018.10.002.

Hanafin, J.A., Quilfen, Y., Ardhuin, F., Sienkiewicz, J., Queffeulou, P., Obrebski, M., Chapron, B., Reul, N., Collard, F., Corman, D., De Azevedo, E.B., Vandemark, D., Stutzmann, E., 2012. Phenomenal sea states and swell from a north atlantic storm in february 2011: a comprehensive analysis. Bull. Am. Meteorol. Soc. 93, 1825–1832. https://doi.org/10.1175/BAMS-D-11-00128.1.

Hanna, S.R., Heinold, D.W., 1985. Development and Application of a Simple Method for Evaluating Air Quality. American Petroleum Institute, Health and Environmental Affairs Dept, Washington, U.S.A. Technical Report.

Hanson, J.L., Phillips, O.M., 2001. Automated analysis of ocean surface directional wave spectra. J. Atmos. Ocean. Technol. 18, 177–293.

Hasselmann, S., Hasselmann, K., Allender, J.H., Barnett, T.P., 1985. Computations and parametrizations of the nonlinear energy transfer in a gravity-wave spectrum, Part II: parametrization of the nonlinear energy transfer for application in wave models. J. Phys. Oceanogr. 15 (1), 378–391.

Hersbach, H., Bell, B., Berrisford, P., Hirahara, S., Horányi, A., Muñoz-Sabater, J., Nicolas, J., Peubey, C., Radu, R., Schepers, D., Simmons, A., Soci, C., Abdalla, S., Abellan, X., Balsamo, G., Bechtold, P., Biavati, G., Bidlot, J., Bonavita, M., De Chiara, G., Dahlgren, P., Dee, D., Diamantakis, M., Dragani, R., Flemming, J., Forbes, R., Fuentes, M., Geer, A., Haimberger, L., Healy, S., Hogan, R.J., Hólm, E., Janisková, M., Keeley, S., Laloyaux, P., Lopez, P., Lupu, C., Radnoti, G., de Rosnay, P., Rozum, I., Vamborg, F., Villaume, S., Thépaut, J.N., 2020. The ERA5 global reanalysis. Q. J. R. Meteorol. Soc. 146, 1999–2049. https://doi.org/10.1002/qj.3803.

Janssen, P.A.E.M., 1991. Quasi-linear theory of wind-wave generation applied to wave forecasting. J. Phys. Oceanogr. 21 (11), 1631–1642 https://doi.org/10.1175/1520-0485(1991)021<1631:qltoww>2.0.co;2.

Kendall, M., 1975. Rank Correlation Method, fourth ed. Charles Griffin, London.

Li, N., Cheung, K.F., Stopa, J.E., Hsiao, F., Chen, Y.L., Vega, L., Cross, P., 2016. Thirty-four years of Hawaii wave hindcast from downscaling of climate forecast system reanalysis. Ocean Model. 100, 78–95. https://doi.org/10.1016/j.ocemod.2016.02.001.

Lionello, P., Sanna, A., 2005. Mediterranean wave climate variability and its links with NAO and Indian Monsoon. Clim. Dynam. 25, 611–623. https://doi.org/10.1007/s00382-005-0025-4.

Lira-loarca, A., Cáceres-euse, A., De-leo, F., Besio, G., 2022. Wave modeling with unstructured mesh for hindcast , forecast and wave hazard applications in the Mediterranean Sea. Appl. Ocean Res. 122, 103118 https://doi.org/10.1016/j.apor.2022.103118.

Mann, H.B., 1945. Nonparametric tests against trend. Econometrica 13, 245–259. https://doi.org/10.2307/1907187.
Martínez-Asensio, A., Marcos, M., Jordà, G., Gomis, D., 2013. Calibration of a new wind-wave hindcast in the Western Mediterranean. J. Mar. Syst. 121–122, 1–10. https://doi.org/10.1016/j.jmarsys.2013.04.006.
Meehl, G.A., Senior, C.A., Eyring, V., Flato, G., Lamarque, J.F., Stouffer, R.J., Taylor, K. E., Schlund, M., 2020. Context for interpreting equilibrium climate sensitivity and transient climate response from the CMIP6 Earth system models. Sci. Adv. 6, 1–11. https://doi.org/10.1126/sciadv.aba1981.
Melet, A., Meyssignac, B., Almar, R., Le Cozannet, G., 2018. Under-estimated wave contribution to coastal sea-level rise. Nat. Clim. Change 8, 234–239. https://doi.org/10.1038/s41558-018-0088-y.
Mentaschi, L., Besio, G., Cassola, F., Mazzino, A., 2015. Performance evaluation of wavewatch III in the Mediterranean Sea. Ocean Model. 90, 82–94. https://doi.org/10.1016/j.ocemod.2015.04.003.
Morales-Márquez, V., Orfila, A., Simarro, G., Marcos, M., 2020. Extreme waves and climatic patterns of variability in the eastern North Atlantic and Mediterranean basins. Ocean Sci. 16, 1385–1398. https://doi.org/10.5194/os-16-1385-2020.
Musić, S., Nicković, S., 2008. 44-year wave hindcast for the Eastern Mediterranean. Coast. Eng. 55, 872–880. https://doi.org/10.1016/j.coastaleng.2008.02.024.
Pallares, E., Sánchez-Arcilla, A., Espino, M., 2014. Wave energy balance in wave models (SWAN) for semi-enclosed domains-Application to the Catalan coast. Continent. Shelf Res. 87, 41–53. https://doi.org/10.1016/j.csr.2014.03.008.
Passaro, M., Fenoglio-Marc, L., Cipollini, P., 2015. Validation of significant wave height from improved satellite altimetry in the German bight. IEEE Trans. Geosci. Rem. Sens. 53, 2146–2156. https://doi.org/10.1109/TGRS.2014.2356331.
Perez, J., Menendez, M., Losada, I.J., 2017. GOW2: a global wave hindcast for coastal applications. Coast. Eng. 124, 1–11. https://doi.org/10.1016/j.coastaleng.2017.03.005.
Piollé, J.-F., Dodet, G., Quilfen, Y., 2020. ESA Sea State Climate Change Initiative (Sea_State_cci): global remote sensing multi-mission along-track significant wave height, L2P prod- uct, version 1.1. Centre for Environmental Data Analysis. https://doi.org/10.5285/f91cd3ee7b6243d5b7d41b9beaf397e1, 2020a.
Ponce de León, S., Guedes Soares, C., 2008. Sensitivity of wave model predictions to wind fields in the Western Mediterranean sea. Coast. Eng. 55, 920–929. https://doi.org/10.1016/j.coastaleng.2008.02.023.
Rascle, N., Ardhuin, F., 2013. A global wave parameter database for geophysical applications. Part 2: model validation with improved source term parameterization. Ocean Model. 70, 174–188. https://doi.org/10.1016/j.ocemod.2012.12.001.
Reguero, B.G., Menéndez, M., Méndez, F.J., Mínguez, R., Losada, I.J., 2012. A Global Ocean Wave (GOW) calibrated reanalysis from 1948 onwards. Coast. Eng. 65, 38–55. https://doi.org/10.1016/j.coastaleng.2012.03.003.
Ribal, A., Young, I.R., 2019. 33 Years of globally calibrated wave height and wind speed data based on altimeter observations. Sci. Data 6, 1–15. https://doi.org/10.1038/s41597-019-0083-9.
Ridal, M., Olsson, E., Unden, P., Zimmermann, K., Ohlsson, A., 2017. Uncertainties in Ensembles of Regional Re-analyses - Deliverable D2.7 HARMONIE Reanalysis Report of Results and Dataset. http://www.uerra.eu/component/dpattachments/?task=attachment.download&id=296.
Saha, S., Moorthi, S., Pan, H.L., Wu, X., Wang, Jiande, Nadiga, S., Tripp, P., Kistler, R., Woollen, J., Behringer, D., Liu, H., Stokes, D., Grumbine, R., Gayno, G., Wang, Jun, Hou, Y.T., Chuang, H.Y., Juang, H.M.H., Sela, J., Iredell, M., Treadon, R., Kleist, D., Van Delst, P., Keyser, D., Derber, J., Ek, M., Meng, J., Wei, H., Yang, R., Lord, S., Van Den Dool, H., Kumar, A., Wang, W., Long, C., Chelliah, M., Xue, Y., Huang, B., Schemm, J.K., Ebisuzaki, W., Lin, R., Xie, P., Chen, M., Zhou, S., Higgins, W., Zou, C. Z., Liu, Q., Chen, Y., Han, Y., Cucurull, L., Reynolds, R.W., Rutledge, G., Goldberg, M., 2010. The NCEP climate forecast system reanalysis. Bull. Am. Meteorol. Soc. 91, 1015–1057. https://doi.org/10.1175/2010BAMS3001.1.
Saha, S., Moorthi, S., Wu, X., Wang, J., Nadiga, S., Tripp, P., Behringer, D., Hou, Y.T., Chuang, H.Y., Iredell, M., Ek, M., Meng, J., Yang, R., Mendez, M.P., Van Den Dool, H., Zhang, Q., Wang, W., Chen, M., Becker, E., 2014. The NCEP climate forecast system version 2. J. Clim. 27, 2185–2208. https://doi.org/10.1175/JCLI-D-12-00823.1.
Sánchez-Arcilla, A., González-Marco, D., Bolānos, R., 2008. A review of wave climate and prediction along the Spanish Mediterranean coast. Nat. Hazards Earth Syst. Sci. 8, 1217–1228. https://doi.org/10.5194/nhess-8-1217-2008.
Scott, F., Antolinez, J.A.A., McCall, R., Storlazzi, C., Reniers, A., Pearson, S., 2020. Hydro-morphological characterization of coral reefs for wave runup prediction. Front. Mar. Sci. 7 https://doi.org/10.3389/fmars.2020.00361. Article 361.
Shimura, T., Mori, N., 2019. High-resolution wave climate hindcast around Japan and its spectral representation. Coast. Eng. 151, 1–9. https://doi.org/10.1016/j.coastaleng.2019.04.013.
Soran, M.B., Amarouche, K., Akpınar, A., 2022. Spatial calibration of WAVEWATCH III model against satellite observations using different input and dissipation parameterizations in the Black Sea. Ocean Eng 257, 111627. https://doi.org/10.1016/j.oceaneng.2022.111627.
Sorensen, O.R., Kofoed-Hansen, H., Rugbjerg, M., Sorensen, L.S., 2004. A third generation spectral wave model using an unstructured finite volume technique. September 2004. In: Proceedings of the 29th International Conference of Coastal Engineering, vols. 19–24 (Lisbon, Portugal).
Stopa, J.E., 2018. Wind forcing calibration and wave hindcast comparison using multiple reanalysis and merged satellite wind datasets. Ocean Model. 127, 55–69. https://doi.org/10.1016/j.ocemod.2018.04.008.
Stopa, J.E., Ardhuin, F., Babanin, A., Zieger, S., 2016. Comparison and validation of physical wave parameterizations in spectral wave models. Ocean Model. 103, 2–17. https://doi.org/10.1016/j.ocemod.2015.09.003.
Stopa, J.E., Ardhuin, F., Stutzmann, E., Lecocq, T., 2019. Sea State trends and variability: consistency between models, altimeters, buoys, and Seismic data (1979–2016). J. Geophys. Res. Ocean. 124, 3923–3940. https://doi.org/10.1029/2018JC014607.
Taylor, K.E., 2001. Summarizing multiple aspects of model performance in a single diagram. J. Geophys. Res. 106 (106), 1984–2012.
The WAVEWATCH III® Development Group (WW3DG), 2019. User Manual and System Documentation of WAVEWATCH III® Version 6.07. Tech. Note 333. NOAA/NWS/NCEP/MMAB, College Park, MD, USA, p. 465 (Appendices).
Tolman, H.L., 2002. Alleviating the garden sprinkler effect in wind wave models. Ocean Model. 4, 269–289. https://doi.org/10.1016/S1463-5003(02)00004-5.
Toomey, T., Amores, A., Marcos, M., Orfila, A., 2022. Coastal sea levels and wind-waves in the Mediterranean Sea since 1950 from a high-resolution ocean reanalysis. Front. Mar. Sci. 9, 1–16. https://doi.org/10.3389/fmars.2022.991504.
Tracy, B., Devaliere, E.-M., Nicolini, T., Tolman, H.L., Hanson, J.L., 2007. Wind sea and swell delineation for numerical wave modeling. In: 10th International Workshop on Wave Hindcasting and Forecasting & Coastal Hazards Symposium, JCOMM Tech. Rep., vol. 41. WMO/TD-No. 1442, Paper P12.
Umesh, P.A., Behera, M.R., 2020. Performance evaluation of input-dissipation parameterizations in WAVEWATCH III and comparison of wave hindcast with nested WAVEWATCH III-SWAN in the Indian Seas. Ocean Eng 202, 106959. https://doi.org/10.1016/j.oceaneng.2020.106959.
Uppala, S.M., Kållberg, P.W., Simmons, A.J., Andrae, U., da Costa Bechtold, V., Fiorino, M., Gibson, J.K., Haseler, J., Hernandez, A., Kelly, G.A., Li, X., Onogi, K., Saarinen, S., Sokka, N., Allan, R.P., Andersson, E., Arpe, K., Balmaseda, M.A., Beljaars, A.C.M., van de Berg, L., Bidlot, J., Bormann, N., Caires, S., Chevallier, F., Dethof, A., Dragosavac, M., Fisher, M., Fuentes, M., Hagemann, S., Hólm, E., Hoskins, B.J., Isaksen, L., Janssen, P.A.E.M., Jenne, R., McNally, A.P., Mahfouf, J.F., Morcrette, J.J., Rayner, N.A., Saunders, R.W., Simon, P., Sterl, A., Trenberth, K.E., Untch, A., Vasiljevic, D., Viterbo, P., Woollen, J., 2005. The ERA-40 re-analysis. Q. J. R. Meteorol. Soc. 131, 2961–3012. https://doi.org/10.1256/qj.04.176.
Van Vledder, G.P., Akpinar, A., 2015. Wave model predictions in the Black Sea: sensitivity to wind fields. Appl. Ocean Res. 53, 161–178. https://doi.org/10.1016/j.apor.2015.08.006.
Vannucchi, V., Taddei, S., Capecchi, V., Bendoni, M., Brandini, C., 2021. Dynamical downscaling of era5 data on the north-western mediterranean sea: from atmosphere to high-resolution coastal wave climate. J. Mar. Sci. Eng. 9, 1–29. https://doi.org/10.3390/jmse9020208.
Vincent, L., Soille, P., 1991. Watersheds in digital spaces: an efficient algorithm based on immersion simulations. IEEE Trans. Pattern Anal. Mach. Intell. 13, 583–598.
Vousdoukas, M.I., Mentaschi, L., Voukouvalas, E., Verlaan, M., Feyen, L., 2017. Extreme sea levels on the rise along Europe's coasts. Earth's Future 5, 304–323. https://doi.org/10.1002/2016EF000505.
WAMDI Group, 1988. The WAM model - a third generation ocean wave prediction model. J. Phys. Oceanogr. 18, 1775–1810. http://journals.ametsoc.org/doi/pdf/10.1175/1520-0485%281988%29018%3C1775%3ATWMTGO%3E2.0.CO%3B2.
Wessel, P., Smith, W.H.F., 1996. A global self-consistent, hierarchical, high-resolution shoreline database. J. Geophys. Res. 101 (#B4), 8741–8743. https://doi.org/10.1029/96JB00104, 1996.
Wiegel, M., de Boer, W., van Koningsveld, M., van der Hout, A., Reniers, A., 2021. Global mapping of Seaport operability risk indicators using open-source Metocean data. J. Mar. Sci. Eng. 9, 695. https://doi.org/10.3390/jmse9070695.
Willmott, C.J., Ackleson, S.G., Davis, R.E., Feddema, J.J., Klink, K.M., Legates, D.R., O'Donnell, J., Rowe, C.M., 1985. Statistics for the evaluation and comparison of models. J. Geophys. Res. 90, 8995–90052.
Zecchetto, S., De Biasio, F., 2007. Sea surface winds over the Mediterranean basin from satellite data (2000-04): Meso- and local-scale features on annual and seasonal time scales. J. Appl. Meteorol. Climatol. 46, 814–827. https://doi.org/10.1175/JAM2498.1.